DTU Library

Automated modal parameter estimation for coupled rotor–foundation systems using seal forces as excitation source

Paulsen, Thomas T.; Damsgaard, Sebastian V.; Santos, Ilmar F.

Link back to DTU Orbit

Automated modal parameter estimation for coupled rotor–foundation systems using seal forces as excitation source

Thomas T. Paulsen, Sebastian V. Damsgaard, Ilmar F. Santos *

Department of Civil and Mechanical Engineering, Technical University of Denmark, Koppels Allé 404, Kgs. Lyngby 2800, Denmark

ARTICLE INFO

ABSTRACT

Modal analysis techniques are widely used to characterize vibrations in structures, vehicles, machinery, etc. Modal parameters obtained through modal analysis are useful for structural health monitoring and condition monitoring. The common goal is to ensure the integrity of a mechanical system through monitoring of different operational conditions. Operational conditions described by spatial measurements can for instance be used to observe the vibration characteristics of the system and its parts. Therefore, the main originality of this work is to experimentally investigate if the presence of a turbulent gas flow in seal geometries can facilitate operational modal analysis for a coupled rotor–foundation system. A consistent and automatic way of obtaining the vibration characteristics is necessary to be included in the monitoring schemes. Therefore, this work also proposes a method to automatically obtain modal parameters for a bed plate of a rotor–foundation system when the rotor is affected by active magnetic bearings and gas seals. The automatic modal parameter algorithm is built on the stabilization diagram of modal parameters obtained from the stochastic subspace identification. Intermediate results from the automatic modal parameter algorithm show that some of the distance measures i.e., $d\omega_{n,d}$, $d\zeta$, $dMACX$, $d\lambda$, $dMACX_{\omega_{n,d}}$, $dMACX_\zeta$, and $dMACX_\lambda$, for modal parameters in a stabilization diagram are better suited than others when distinguishing between possible physical modes and certainly spurious poles. The frequency band of interest for the system is found to influence the number of possible physical modes identified by the automatic algorithm. Measurements from 13 roving accelerometers are combined with the automatic modal parameter algorithm to obtain the vibration characteristics of the rotor and bed plate. For different operational conditions in the seal geometry, seven modes are consistently identified as physical modes by the automatic modal parameter algorithm. The algorithm uses (i) a combination of a white noise disturbance pattern intentionally introduced into the system through the active magnetic bearings and (ii) the operational disturbance coming from the seals, non-intentionally introduced by the turbulent gas flow. The seven physical modes are also identified when (iii) the rotor–foundation system is only disturbed from the turbulent gas flow in the seals. The seven physical modes identified by the algorithm under conditions (i), (ii), and (iii) compare well to the vibration characteristics found in experiments via experimental modal analysis and impact hammer testing as well as via a mathematical model of the rotor–foundation system.

* Corresponding author.
  E-mail addresses: ththpa@dtu.dk (T.T. Paulsen), s184162@student.dtu.dk (S.V. Damsgaard), ilsa@dtu.dk (I.F. Santos).

1. Introduction

Modal parameters are used to mathematically describe vibration characteristics in mechanical systems. The modal parameters help indicate whether a system is behaving as intended. Traditional modal test methods are presented in [1]. These are often referred to as Experimental Modal Analysis (EMA) and require the operational conditions to be well-known and disturbances to be measured. This often means that the system will be operated differently than normal during the modal tests. For instance in [2], Bidaut et al. mounted an additional shaker unit to precisely know the disturbances imposed on the system. Therefore, EMA is commonly used when systems are commissioned. Methods that do not require full knowledge about the disturbance are commonly known as Operational Modal Analysis (OMA). An introduction to the concepts of OMA and well-known methods is provided in [3]. The OMA methods require some a priori knowledge about the statistical nature of the disturbance which is often assumed to be described by Gaussian distributed white noise. In [4], a review of existing methods and common assumptions used in different modal parameter estimation methods, including OMA methods, is provided. It also provides the user with some rules of thumb for carrying out experiments to perform modal parameter identification.

For structures such as bridges and high-rise buildings, vibration amplifications are investigated both for the sake of structural integrity and comfort. In [5], an analysis of a high storage timber building is investigated for comfort during wind loadings to ensure that the building can be used as intended. Such systems are affected by multiple loading cases that are difficult to estimate and even harder to measure during vibration tests. Therefore, the OMA methods have been a necessary tool to estimate the vibration characteristics of these structures. In the case of moving structures such as vehicles and vessels, the dynamical properties, i.e. vibration characteristics, might experience great changes between the operating and the stationary states. Hermans and Van der Auweraer [6] tested flutter data at different air speeds to show the system changes from new operational conditions. When a structure is in operational conditions, methods that are applicable without an explicit estimation of present excitation patterns will have higher chances of providing a good estimate of the vibration characteristics without impacting the intended use. The need for OMA methods to estimate modal parameters has pushed the development of multiple methods. Many of the basic concepts related to the methods are described in [3,4]. However, even when one has chosen an OMA method to use, that method requires a choosing of parameters and method specific analyses before modal parameter estimations are obtained. In [7], experimental data from an arch bridge is used to provide a tutorial on the use of different OMA methods with highlights of method specific analyses. The OMA methods are sensitive to the choosing of the parameters related to the methods. Therefore, it is common for users to do a short study of the impact on the estimations from the parameters chosen for the method before choosing the parameters to use for analysing experimental data. In [8], Reynders first tested the effect of uncertainties in modal parameter estimates from variations in the model parameters through a numerical example. Hereafter, the estimated uncertainties were used to test the effect of a destructive loading case for a concrete beam on modal parameter estimates and their uncertainties. Saint Martin et al. [9] present the use of unbalance force disturbance in a rotating machine to identify the vibration characteristics of the supporting structure. Changes to the supporting structure are found to impact the vibration characteristics which is captured using an OMA method. These examples showcase the use of modal parameters such as natural frequency and mode shape vector as identifiers to system changes.

In the related research fields of Structural Health Monitoring (SHM) and Condition Monitoring (CM), the modal parameters are used among other indicators to track structural changes over time that are not just caused by changes in the environment. An introduction to the SHM is described in [10] and a handbook of CM is provided in [11], while a review investigating the heading of the research within the field of CM is presented in [12]. The fields are similar in the way that both search to determine the remaining life and to prevent critical failures in mechanical systems. However, SHM focuses on civil structures and CM focuses on rotating machinery. Structural changes happen due to different causes, e.g. corrosion, heavy loads, earthquakes, etc. The indicators provide useful insight into the structural and functional integrity over time and help in decision making about maintenance problems. In SHM and CM setups, algorithms that are fully automated in the process of extracting modal parameters are necessary to continuously evaluate the vibration characteristics and changes hereof if these are to be used in the evaluation of the structural or functional integrity. In [13], Magalhães et al. presented an automated OMA algorithm applied to the dynamic characterization of a bridge. The algorithm calculates a distance measure to define differences between modal parameter estimates. The modal parameters are used to group identified modes through the hierarchical cluster algorithm based on their similarities in natural frequency and mode shape vector. Finally, modes with outlying estimations of damping are neglected and the mean value of the modal parameter estimates describing a mode is used as the resulting modal parameter estimate. A similar approach is presented in [14]. Here, an additional step of a K-means clustering using soft validation criteria for modal parameter estimates separates possible physical modes and certainly spurious poles. Next, hard criteria are used to eliminate certainly spurious poles that were wrongly encapsulated in the group of possible physical modes. The modal parameters defined as certainly spurious poles are cleared from the stabilization diagram before a hierarchical clustering algorithm is used. After the hierarchical clustering, one representative modal parameter estimate is chosen as the resulting mode estimator of each group. In [15], Neu et al. present a multi-stage clustering algorithm using a K-means and hierarchical clustering algorithm for dynamic characterization of a glass fibre specimen. Here, a distance measure based on a combination of the eigenvalue and modal assurance criterion is used to distinguish estimated modes. The presented method required no inputs or thresholds from a user. Charbonnel [16] presents fuzzy c-means algorithms to separate possible physical modes and spurious poles better before using a hierarchical clustering algorithm. The method is tested on measurements from the shaking-table test campaign. Mugnaini et al. [17] present a data-driven clustering approach for an Automatic OMA algorithm that distinguish modes from the known phenomenon of pole splitting when the model order increases to high numbers in a stabilization diagram. The algorithm is applied to characterize the dynamics of a helicopter blade. In [18], Tronci et al. described a semi-automatic methodology for extracting the modal parameters using two different parametric system identification techniques combined with three clustering

options: two "blind" versions of the commonly used K-means algorithm and a newly developed Density-Based Spatial Clustering of Applications with Noise (DBSCAN). The results demonstrated excellent accuracy and robust performance of the methodology, even in the presence of closely spaced modes for all clustering algorithms. In this paper, the K-means algorithm combined with a hierarchical clustering is chosen. A lot of other approaches for automating the modal parameter choosing process have been provided. For instance in [19], Covioli and Coppotelli presented an automated modal analysis algorithm based on Gaussian mixture models to obtain modal parameter estimates from flight vibration data. Also, Zeng and Hu [20] have tested the use of Gaussian mixture models on vibration data from a four-storage building and a bridge. Priou et al. [21] use the variations of the modal parameters from stochastic subspace methods as formulated in [22,23] to automatically clear out stabilization diagrams and test the algorithm on data from the S101 and Z24 bridge data sets.

The identification of vibration characteristics for rotating machines is the focus of this work where vibration signals from rotor positions and acceleration signals from the supporting structure of the machine elements are analysed. By roving one accelerometer over the supporting structure, the vibration characteristics of the structure are estimated. The goal of the work is to automatically obtain an estimate of the vibration characteristics from ambient excitations in the machine induced by the turbulent gas flow in the seal geometries. An OMA method in the form of Stochastic Subspace Identification (SSI) is chosen to analyse the vibration signals from the ambient excitations. The automated modal parameter identification algorithm is referred to as Automated Operational Modal Analysis (AOMA) in the following. The SSI method can generate a set of modal parameter estimates using an incremental model order for the modal parameter estimation process. Since this is a possibility for many methods, the proposed automated process of modal parameter choosing in the set of modal parameter estimates can be used for different modal parameter estimation methods. The proposed AOMA is founded on the work from [14] since it provided a simple method with the possibility of easily adding distance measures into the automated procedure. The AOMA includes a method for clearing the stabilization diagram for certainly spurious poles that are estimated for example due to noise in the measurement signals. The remaining modal parameters are sorted in a hierarchical clustering algorithm that groups modal parameters that describe the same mode. Groups that contain a high number of possible physical modes are said to have a higher probability of resembling physical modes present in the system. Therefore, groups of possible physical modes that contain fewer possible physical modes than a defined threshold are disregarded as non-physical. A resulting set of modal parameters representing the physical mode contained in each group is calculated by weighting the modal parameters. In this work, the weighting of the modal parameters is based on a comparison of the estimated modal parameters through a modal assurance criterion as presented in [24]. Since the AOMA is used for several roving experiments, the information from each roving experiment needs to be combined using an experiment as a reference. Each experiment is in turn chosen as a reference since any roving experiment could be chosen as the reference. Thereby, a set of physical modes describing the complete vibration characteristics is generated for each roving experiment. The physical modes are combined and analysed through the hierarchical clustering algorithm using the same controls as for the individual roving experiments. The groups that contain the most physical modes are used to calculate the resulting modal parameters through the same weighting process as for the individual roving experiments. The main contributions of this work related to the automation of modal parameter estimations are the use of a weighting between the estimated modal parameters to reduce the contribution to the resulting modal parameter estimate from outlying estimations and the automated combination of modal parameters estimated from different roving experiments to generate a complete vibration pattern.

The main originality of this work is to experimentally investigate and prove that the excitation forces coming from the turbulent flow in gas seals can facilitate operational modal analysis for a rotor–foundation system. The proposed AOMA is evaluated for three different operational conditions (i) introducing deliberately a white noise disturbance pattern into the system through the active magnetic bearings, (ii) combining the magnetic bearing excitation with the operational disturbance coming from the seals non-intentionally induced by the turbulent gas flow, and (iii) using only the operational disturbances from the seals. The outcomes from the AOMA are compared and validated against (a) the estimation of vibration characteristics aided by EMA and (b) predicted by a mathematical model of the test rig derived in [25]. The estimated vibration characteristics of the system are highly correlated even when considering only ambient excitations from a seal geometry.

The article is composed of a description of the experiments and the analyses used in the work followed by a walk-through of the AOMA algorithm using experimental data. Lastly, a comparison between expectations and obtained modal parameter values is presented for all experimental studies.

2. Test facility and experimental testing

The experiments are carried out using a seal force test facility located in a laboratory facility at the Department of Civil and Mechanical Engineering, Technical University of Denmark. Fig. 1 pictures the test setup and the test facility. The test facility illustrated in Fig. 1(b) consists of an electric motor connected to a drive shaft through a belt drive. The drive shaft controls the main rotor through a flexible coupling. The main rotor is levitated in its lateral directions by active magnetic bearings and influenced by two smooth annular seals mounted in a back-to-back configuration. The modules carrying the motor, drive shaft, active magnetic bearings, and seal geometries are situated on a bed plate. The test facility is presented in detail in [26]. The investigation presented in this work focuses mainly on the identification of vibration patterns present in the bed plate of the test facility when the seal inlet pressure changes as described in Table 1. Experimental studies using an excitation hammer are carried out to obtain a benchmark estimate of which vibration patterns are present in the test facility. The excitation patterns (i) generated by the hammer are measured and denoted as known and deterministic. In these experiments, force input signals from the hammer, accelerations from the stationary accelerometer, and operational conditions in the seal geometries are measured. The hammer roves over each
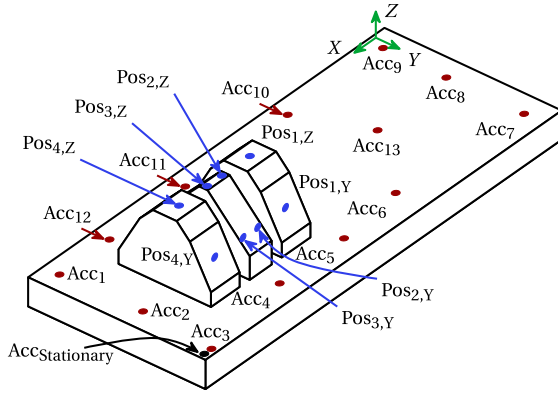
(a) Sketch of points used to estimate vibration characteristics experimentally including position measurements (blue) for the Y- and Z-directions in four positions along the main rotor Pos$_{\#,Y/Z}$, 13 roving accelerometer positions (red) Acc$_{\#}$, and a stationary accelerometer (black) Acc$_{Stationary}$. The coordinate system is presented in green.
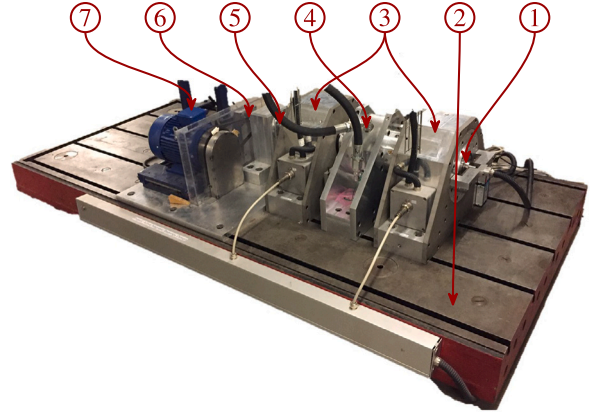
(b) Picture of the seal force test facility including ① the main rotor, ② a flexible foundation, ③ radial active magnetic bearings, ④ plain annular seal geometries in a back-to-back configuration, ⑤ flexible coupling, ⑥ drive shaft, ⑦ electrical motor.

Fig. 1. Presentation of test facility including (a) experimental setup indicating measurement points for EMA and OMA experiments and (b) presentation of components in the test facility. (b) is also presented in [25]. (For interpretation of the references to colour in this figure legend, the reader is referred to the web version of this article.)

Table 1
Experimental test conditions tested in the lab in terms of seal inlet pressure, excitation pattern from the AMBs. The rotational speed of the main rotor is 0 RPM for all experiments.

Test configurations	(a)	(b)	(c)	(d)	(e)	(f)
Pressure [bar]	0	0	1.3	1.3	2.7	2.7
AMB excitation	No	Yes	No	Yes	No	Yes

accelerometer position that are presented in Fig. 1(a). For each tested point, frequency response functions are calculated from 20 measurements of 5 s using a sampling frequency of 3012 Hz. The hammer tests are conducted for experimental test conditions **(a)**, **(c)**, and **(e)**. Additional experiments rely only on the excitation from measurement noise in the sensors and process noise in the control of the active magnetic bearings or from turbulent gas flow in the seal geometries installed in the test facility. These excitation patterns (ii) are unknown but assumed stochastic in the form of Gaussian white noise. Experiments with an imposed pseudo random binary signal as feed forward in the controlling current of the active magnetic bearings are used to magnify the vibrations that should be visible through the normal operating conditions as well. The signals measured in these tests are accelerations from one roving accelerometer and one stationary accelerometer, position signals in Y- and Z-directions of the rotor from hall-effect sensors mounted at four locations, and operational conditions in the seals. The accelerometer is roved through the 13 accelerometer positions presented in Fig. 1(a). The experimental signals for the excitation patterns (ii) are captured for approximately 128 s at a sampling rate of 3012 Hz. These signals are used in the proposed AOMA for test conditions **(b)** through **(f)**.

3. Analysis methodologies

The two types of experiments (i) and (ii) require algorithms built on a different set of assumptions to obtain estimates of modal parameters. Experiments of type (i) require methods within the framework of EMA, while experiments of type (ii) require OMA methods to obtain estimates of modal parameters for the coupled rotor–foundation system. The following highlights first the algorithms within the frameworks of EMA and OMA in sections 3.1 and 3.2. Then a proposed automation of modal parameter choosing from a stabilization diagram is described in Section 3.3.

3.1. EMA algorithm

Experiments of type (i) using the excitation hammer generate well defined frequency response functions from the power spectral densities of the input and output signals calculated from Welch's method [27]. The correlation function $R_{x,y}(\tau)$ between signals $x(t)$ and $y(t)$ is used to calculate the power spectral density $P_{x,y}(\omega)$ of the signals as in Eq. (1).

$$R_{x,y}(\tau) = \lim_{T \to \infty} \frac{1}{T} \int_0^T x(t) \, y(t+\tau) \, \mathrm{d}t, \quad P_{x,y}(\omega) = \frac{1}{2\pi} \int_{-\infty}^{\infty} R_{x,y}(\tau) \exp^{-\sqrt{-1}\,\omega\tau} \, \mathrm{d}\tau \tag{1}$$
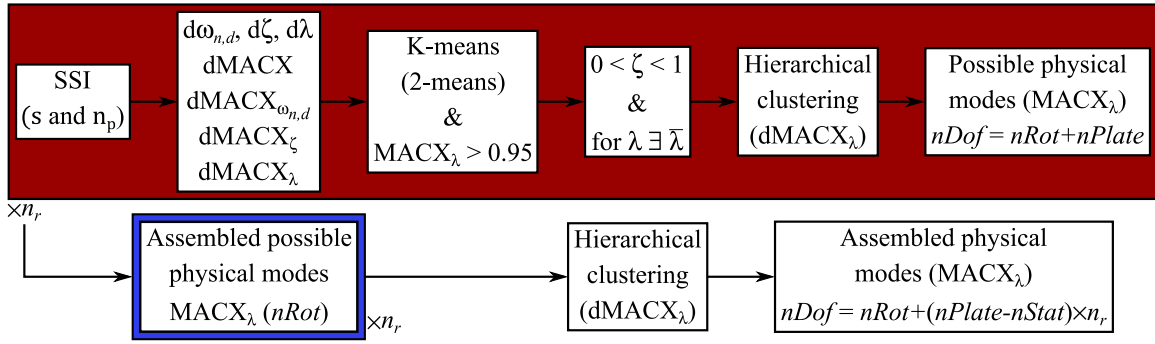
Fig. 2. Graphical presentation of the AOMA algorithm for calculating assembled physical modes. The estimation process for each roving experiment is highlighted in red and the assembling of the possible physical modes between each roving experiment is highlighted in blue. (For interpretation of the references to colour in this figure legend, the reader is referred to the web version of this article.)

The relations between the power spectral densities are calculated as the H_2 estimator for the frequency response functions [28]. The H_2 estimator is chosen since the frequency response function is analysed close to the resonance peaks where the signal to noise ratio is higher for the acceleration signals compared to the input force [29]. The transfer function $H_{x,y}(\omega)$ from input $y(t)$ to output $x(t)$ is calculated as presented in Eq. (2).

$$H_{x,y}(\omega) = \frac{P_{x,x}(\omega)}{P_{x,y}(\omega)} \tag{2}$$

Here, the single degree of freedom curve fitting method, also known as the peak picking method, is used to estimate the modal parameters from the frequency response function. Curve fitting methods to obtain the modal parameter estimates have existed for a long time and are for instance described in [30].

3.2. OMA algorithm

The experiments of type (ii) are analysed using the Stochastic Subspace Identification (SSI) algorithm [31]. The algorithm uses correlation functions $\mathbf{R}(\tau)$ ordered in the form of a Hankel matrix $\mathbf{H}$ using the parameters s and n_p as presented in Eq. (3).

$$\mathbf{H} = \begin{bmatrix} \mathbf{R}(1) & \mathbf{R}(2) & \dots & \mathbf{R}(n_p - 2s + 1) \\ \mathbf{R}(2) & \mathbf{R}(3) & \dots & \mathbf{R}(n_p - 2s + 2) \\ \vdots & \vdots & \ddots & \vdots \\ \mathbf{R}(2s) & \mathbf{R}(2s+1) & \dots & \mathbf{R}(n_p) \end{bmatrix} \tag{3}$$

The Hankel matrix can be computationally efficiently solved through a QR factorization that is used to build a projection matrix $\mathbf{O}_w$. The projection matrix can be expressed as an observability matrix $\mathbf{\Gamma}$ and a matrix of Kalman states $\mathbf{X}$ describing initial conditions of the free decays, which also holds true for the singular value decomposition of $\mathbf{O}_w$. This is mathematically described in Eq. (4).

$$\mathbf{O}_w = \mathbf{U}\,\mathbf{S}\,\mathbf{V}^{\mathrm{T}} = \mathbf{\Gamma}\,\mathbf{X} \tag{4}$$

Here, $\square^{\mathrm{T}}$ denotes the transpose. By calculating the singular value decomposition of the projection matrix, the singular values in the correlation functions can be used to solve for the system matrix of the Kalman states with an incremental model order m using the $2m$ number of most influential singular values [3]. The extraction of the most influential singular values along with the estimation of Kalman states and responses is presented in Eq. (5).

$$\mathbf{U} = \begin{bmatrix} \mathbf{U}_m & \mathbf{U}_r \end{bmatrix}, \quad \mathbf{S} = \begin{bmatrix} \mathbf{S}_m & \mathbf{0} \\ \mathbf{0} & \mathbf{S}_r \end{bmatrix}, \quad \hat{\mathbf{\Gamma}}_m = \mathbf{U}_m\sqrt{\mathbf{S}_m}, \quad \hat{\mathbf{X}}_m = \hat{\mathbf{\Gamma}}_m^{+}\mathbf{O}_w \tag{5}$$

Here, $\square^{+}$ denotes the pseudo-inverse. From the estimates of the Kalman states and responses at different model orders, a set of modal parameters describing a stabilization diagram is obtained.

3.3. Automation of the modal parameter choosing

A method to automate the process of choosing modal parameters that describes physical modes in a rotating machine is proposed. The method assumes that the modal parameter estimation process can generate a set of modal parameters that can be described by a stabilization diagram as is the case for the SSI algorithm. The automation method, which is also graphically described in Fig. 2, calculates distance measures between estimated modes when incrementally increasing the model order. The eigenvalue λ expresses the damped natural frequency $\omega_{n,d} = \mathrm{Im}(\lambda)$ and the damping factor $\zeta = -\mathrm{Re}(\lambda)/|\lambda|$. Thereby, each mode carries information about three features, namely the damped natural frequency, the damping factor, and the mode shape. The distance measures of the mode

shape vectors are based on the extensions to the modal assurance criterion presented in [32]. The distance measures range from considering only the stabilization of one feature at a time to all features simultaneously. Eqs. (6) through (12) present the distance measures considered between mode i from model order m and mode j from model order $m + 1$.

$$d\omega_{n,d,i,j} = \frac{\frac{1}{2}\left|\omega_{n,d,i,m} - \omega_{n,d,j,m+1}\right|}{\max\left(\left[\left|\omega_{n,d,i,m}\right|, \left|\omega_{n,d,j,m+1}\right|\right]\right)} \tag{6}$$

$$d\zeta_{i,j} = \frac{\frac{1}{2}\left|\zeta_{i,m} - \zeta_{j,m+1}\right|}{\max\left(\left[\left|\zeta_{i,m}\right|, \left|\zeta_{j,m+1}\right|\right]\right)} \tag{7}$$

$$d\lambda_{i,j} = \frac{\frac{1}{2}\left|\lambda_{i,m} - \lambda_{j,m+1}\right|}{\max\left(\left[\left|\lambda_{i,m}\right|, \left|\lambda_{j,m+1}\right|\right]\right)} \tag{8}$$

$$\text{MACX}_{i,j} = \frac{\left(\left|\mathbf{v}_{i,m}^*\mathbf{v}_{j,m+1}\right| + \left|\mathbf{v}_{i,m}^T\mathbf{v}_{j,m+1}\right|\right)^2}{\left(\left|\mathbf{v}_{i,m}^*\mathbf{v}_{i,m}\right| + \left|\mathbf{v}_{i,m}^T\mathbf{v}_{i,m}\right|\right)\left(\left|\mathbf{v}_{j,m+1}^*\mathbf{v}_{j,m+1}\right| + \left|\mathbf{v}_{j,m+1}^T\mathbf{v}_{j,m+1}\right|\right)} \tag{9}$$

$$\text{MACX}_{\omega_{n,d},i,j} = \frac{\left(\dfrac{\left|\mathbf{v}_{i,m}^*\mathbf{v}_{j,m+1}\right|}{\left|\omega_{n,d,i,m}\right| + \left|\omega_{n,d,j,m+1}\right|} + \dfrac{\left|\mathbf{v}_{i,m}^T\mathbf{v}_{j,m+1}\right|}{\left|\omega_{n,d,i,m}\right| + \left|\omega_{n,d,j,m+1}\right|}\right)^2}{\left(\dfrac{\left|\mathbf{v}_{i,m}^*\mathbf{v}_{i,m}\right|}{2\left|\omega_{n,d,i,m}\right|} + \dfrac{\left|\mathbf{v}_{i,m}^T\mathbf{v}_{i,m}\right|}{2\left|\omega_{n,d,i,m}\right|}\right)\left(\dfrac{\left|\mathbf{v}_{j,m+1}^*\mathbf{v}_{j,m+1}\right|}{2\left|\omega_{n,d,j,m+1}\right|} + \dfrac{\left|\mathbf{v}_{j,m+1}^T\mathbf{v}_{j,m+1}\right|}{2\left|\omega_{n,d,j,m+1}\right|}\right)} \tag{10}$$

$$\text{MACX}_{\zeta,i,j} = \frac{\left(\dfrac{\left|\mathbf{v}_{i,m}^*\mathbf{v}_{j,m+1}\right|}{\zeta_{i,m} + \zeta_{j,m+1}} + \dfrac{\left|\mathbf{v}_{i,m}^T\mathbf{v}_{j,m+1}\right|}{\zeta_{i,m} + \zeta_{j,m+1}}\right)^2}{\left(\dfrac{\left|\mathbf{v}_{i,m}^*\mathbf{v}_{i,m}\right|}{2\zeta_{i,m}} + \dfrac{\left|\mathbf{v}_{i,m}^T\mathbf{v}_{i,m}\right|}{2\zeta_{i,m}}\right)\left(\dfrac{\left|\mathbf{v}_{j,m+1}^*\mathbf{v}_{j,m+1}\right|}{2\zeta_{j,m+1}} + \dfrac{\left|\mathbf{v}_{j,m+1}^T\mathbf{v}_{j,m+1}\right|}{2\zeta_{j,m+1}}\right)} \tag{11}$$

$$\text{MACX}_{\lambda,i,j} = \frac{\left(\dfrac{\left|\mathbf{v}_{i,m}^*\mathbf{v}_{j,m+1}\right|}{\left|\bar{\lambda}_{i,m} + \lambda_{j,m+1}\right|} + \dfrac{\left|\mathbf{v}_{i,m}^T\mathbf{v}_{j,m+1}\right|}{\left|\lambda_{i,m} + \lambda_{j,m+1}\right|}\right)^2}{\left(\dfrac{\left|\mathbf{v}_{i,m}^*\mathbf{v}_{i,m}\right|}{2\,\text{Re}\left(\lambda_{i,m}\right)} + \dfrac{\left|\mathbf{v}_{i,m}^T\mathbf{v}_{i,m}\right|}{2\left|\lambda_{i,m}\right|}\right)\left(\dfrac{\left|\mathbf{v}_{j,m+1}^*\mathbf{v}_{j,m+1}\right|}{2\,\text{Re}\left(\lambda_{j,m+1}\right)} + \dfrac{\left|\mathbf{v}_{j,m+1}^T\mathbf{v}_{j,m+1}\right|}{2\left|\lambda_{j,m+1}\right|}\right)} \tag{12}$$

Here, $\bar{\square}$ and $\square^*$ denote the complex conjugate and the complex conjugate transpose, respectively. In the following, the distances $d\omega_{n,d,i,j}$, $d\zeta_{i,j}$, and $d\lambda_{i,j}$ will be referred to as dx, while the modal assurance criteria $\text{MACX}_{i,j}$, $\text{MACX}_{\omega_{n,d},i,j}$, $\text{MACX}_{\zeta,i,j}$, and $\text{MACX}_{\lambda,i,j}$ are referred to as MACX_x. All measures are restricted to values between 0 and 1. However, all distances described through the change dx are 0 when there is no distance and 1 when the distance is as large as it can be, while the modal assurance criteria are 0 when the modes are orthogonal and 1 when the modes are parallel. Therefore, the distance of the modal assurance criteria is formulated as $d\text{MACX}_x = 1 - \text{MACX}_x$. In some cases, it will not hold true that all measures will be between 0 and 1. If the denominator in the distance measures dx is 0, the value of the distance is defined as 1. Also, the real part of the parameters $\left|\omega_{n,d,i,m}\right|$ and $\left|\omega_{n,d,j,m+1}\right|$, $\zeta_{i,m}$ and $\zeta_{j,m+1}$, and $-\lambda_{i,m}$ and $-\lambda_{j,m+1}$ are required to be greater than 0. If this is not the case, the measures $d\text{MACX}_{\omega_{n,d},i,j}$, $d\text{MACX}_{\zeta,i,j}$, and $d\text{MACX}_{\lambda,i,j}$ are set to 1, respectively. Distance measures that only evaluate one feature at a time are $d\omega_{n,d,i,j}$, $d\zeta_{i,j}$, and $d\text{MACX}_{i,j}$. Measures that include distance measures between two features at a time are $d\lambda_{i,j}$ (damped natural frequency and damping factor), $d\text{MACX}_{\omega_{n,d},i,j}$ (damped natural frequency and mode shape), and $d\text{MACX}_{\zeta,i,j}$ (damping factor and mode shape). Information about all features is then present in the measure $d\text{MACX}_{\lambda,i,j}$. To determine which set of distance measures are to be used for mode i from model order m, the Euclidean distance $dE_{i,j}$ for all sets of measures is calculated as:

$$dE_{i,j} = \sqrt{d\omega_{n,d,i,j}^2 + d\zeta_{i,j}^2 + d\text{MACX}_{i,j}^2 + d\lambda_{i,j}^2 + d\text{MACX}_{\omega_{n,d},i,j}^2 + d\text{MACX}_{\zeta,i,j}^2 + d\text{MACX}_{\lambda,i,j}^2} \tag{13}$$

The mode j in model $m + 1$ that minimizes the measure of $dE_{i,j}$ is chosen as the mode to be compared to mode i in model order m. The seven distance measures are then used to optimize two centroids initiated from [0 0 0 0 0 0 0] and [1 1 1 1 1 1 1] containing possible physical modes and spurious poles, respectively. When the optimal location for the centroids is found, the set containing spurious poles is cleared out. Additionally, a minimum value of 0.95 is defined for the modal assurance criterion $\text{MACX}_{\lambda,i,j}$ describing the difference between all features in the mode. After the possible physical modes have been identified, another set of measures is used that sorts out certainly spurious poles that erroneously have been labelled possible physical. These measures relate only to the eigenvalue, stating that the mode is only considered physical if the damping is greater than 0 and less
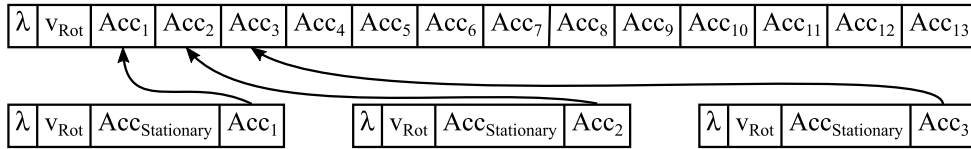
Fig. 3. Assembling modal parameters for complete mode of bed plate.

than 1 and that for every eigenvalue, the complex conjugate of that eigenvalue must exist in the set. In a physical system, over-damped eigenvalues, that have a damping factor equal to 1, may exist. However, the SSI method does not estimate these modes accurately. Therefore, the over-damped modes are excluded from this analysis. The process is carried out in this order to minimize the risk of possible physical poles being wrongly encapsulated in the group of spurious poles. The remaining modal parameters are considered a set of modes that can describe the vibration characteristics of the machine. The last sorting consists of a hierarchical clustering algorithm that computes a distance between all modes in the set chosen as $dMACX_\lambda$. The algorithm combines modes into clusters starting from modes that have the shortest distances. When two clusters of modes are to be combined, it is chosen that the average distance between the members of the clusters is evaluated as the distance between the clusters. A threshold value specifies the distance for which the clusters are defined as different. Some clusters will contain more modes than others. The more modes contained in a cluster, the higher the chance that this is a physical mode. Therefore, clusters with fewer members than a cut-off value are disregarded as spurious poles. Within the resulting clusters, the contribution to the resulting mode from the modal parameters contained in each cluster is defined through a comparison between the modal parameters calculated by $MACX_\lambda$. This process is further described in Section 3.3.1. In this experimental campaign, the resulting modes from the automated method consist of eight degrees of freedom to describe the rotor movements $nRot$ and two degrees of freedom to describe the plate deflections $nPlate$. One degree of freedom for the plate deflections $nStat$ is measured at the same place over multiple experiments, which is used to scale the mode shape. Therefore, this process is repeated for the number of roving experiments used in the campaign defined as n_r, which for this experimental campaign has been chosen as equal to 13.

Another way to tackle the problem of multiple roving experiments could be to derive a power spectral density matrix based on the power spectral densities from a reference degree of freedom. Thereby the algorithm would not need to be applied for each individual roving experiment. The analysis of each roving experiment is however chosen since only simple data processing is required for this method before the SSI algorithm can be applied.

When the AOMA algorithm has generated modes for all n_r experiments, each resulting mode contains a piece of information of the complete mode shape. However, that information needs to be matched between the experiments as illustrated for the first three roving experiments in Fig. 3. Here, the modal coordinate vector is normalized using the $Acc_{Stationary}$ position. Then, a roving experiment is chosen as the reference and the eigenvalue and modal vector describing the rotor degrees of freedom are used to pair the information of the roving accelerometer positions based on a comparison through $MACX_\lambda$. The information from the mode that compares best to the reference mode is used to construct the complete mode shape. Since all matched modes include information of the eigenvalue and rotor mode shape vector, this information is merged into one estimate for the complete mode. This is done by averaging the eigenvalue and rotor modal components based on the weighting method described in 3.3.1 after the mode shape components have been paired. Any roving experiment could be chosen as the reference. Therefore, all experiments are in turn used as the reference. It means that the step of pairing the estimated modes from each roving experiment, marked in blue in Fig. 2, is repeated n_r times. This procedure results in a set of modes that in some cases are similar to others and in other cases are unique. The more modes that one mode compares well to, the higher the chance that this mode is indeed describing a physical mode. For this reason, another hierarchical clustering is chosen to generate clusters that contain comparable modes. The procedure is chosen similar to that used in the initial modal parameter choosing algorithm. In the final clusters, the weighting obtained from the comparison between the modes through $MACX_\lambda$ is used to scale the contributions from the modal parameters to the resulting mode.

3.3.1. Weighting from modal assurance criteria

A method weighting contributions from multiple modes is chosen to calculate a resulting mode. The weightings are based on a comparison through a modal assurance criterion. In [24], it was shown that the method increases the accuracy of the resulting mode. In this work, the weighting is obtained by comparing the modes in a cluster using the modal assurance criterion $MACX_\lambda$. The mode that compares well to most of the modes is given the highest weight and the worse a mode compares to the other modes in the set, the lower the weighting given. Fig. 4 presents graphically the method that generates a symmetric matrix with ones along the diagonal. The matrix is summed through its rows and scaled by the maximum values. The procedure results in a vector containing values between 0 and 1 which define the contribution to the resulting mode from each mode contained in the cluster.

4. Results of the automated vibration characterization method

The results of the estimated vibration characteristics are presented in four parts. First, the focus is turned to the AOMA algorithm and the challenges that lie in the automation of the process. The challenges are described through a presentation of intermediate results from the automation method in 4.1. The estimated vibration characteristics from the AOMA algorithm are then compared to the characteristics estimated by the EMA method and the mathematical model of the test facility in 4.2. An analysis of the impact on the identified physical modes caused by changes to the parameters used in the modal parameter estimation method SSI and operational conditions in the seal geometry is presented in 4.3.
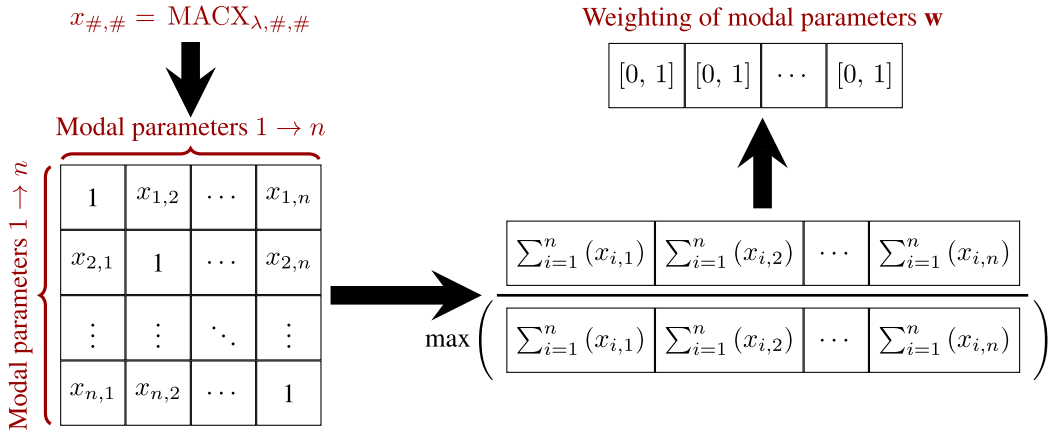
$$x_{\#,\#} = \text{MACX}_{\lambda,\#,\#}$$

Weighting of modal parameters **w**

$[0,\ 1]$	$[0,\ 1]$	$\cdots$	$[0,\ 1]$

Modal parameters $1 \rightarrow n$

1	$x_{1,2}$	$\cdots$	$x_{1,n}$
$x_{2,1}$	1	$\cdots$	$x_{2,n}$
$\vdots$	$\vdots$	$\ddots$	$\vdots$
$x_{n,1}$	$x_{n,2}$	$\cdots$	1

$$\max\left(\frac{\sum_{i=1}^{n}(x_{i,1}) \quad \sum_{i=1}^{n}(x_{i,2}) \quad \cdots \quad \sum_{i=1}^{n}(x_{i,n})}{\sum_{i=1}^{n}(x_{i,1}) \quad \sum_{i=1}^{n}(x_{i,2}) \quad \cdots \quad \sum_{i=1}^{n}(x_{i,n})}\right)$$

Fig. 4. Graphical presentation of modal parameter weighting method with inspiration from [24].
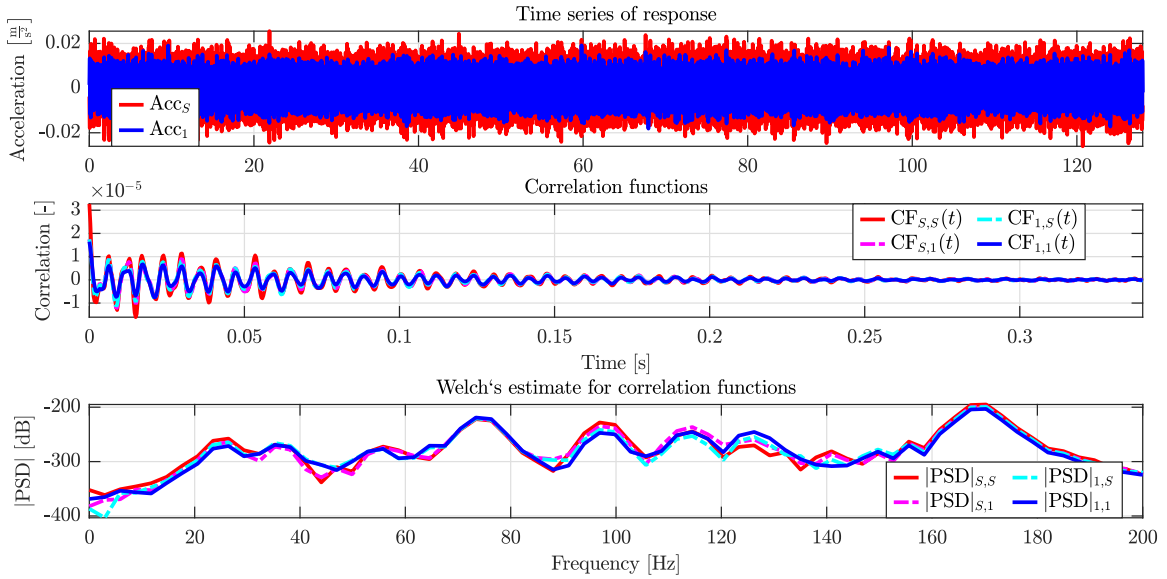

Fig. 5. Presentation of experimental signals and correlation functions for accelerometer signals from the stationary accelerometer Acc_S and the roving accelerometer in position 1 Acc_1 under test conditions **(b)**. The correlation function is analysed in the frequency domain using Welch's estimate. The Hanning window is imposed on the signal for the analysis using one block.

4.1. Intermediate results from the AOMA algorithm

The AOMA algorithm is applied for each roving experiment. The intermediate results from the experiment with the roving accelerometer at Acc_1 under test conditions **(b)** are presented in the following. The experimental acceleration signals and resulting correlation functions are presented along with an analysis of the frequency contents in the correlation signals in Fig. 5. The acceleration signals correspond to a white Gaussian noise signal which is optimal to be analysed in the OMA framework. The correlation function is presented with 0 to 1023 time lags. The correlation is highest when no time lags are introduced and reduce in the form of a free decay as the time lags increase. This is the expected behaviour of the correlation functions. The frequency contents in the correlation functions are also shown. The correlation functions are analysed through Welch's estimate using the Hanning window over one block. Some peaks around the frequencies 26 Hz, 35 Hz, 56 Hz, 73 Hz, 97 Hz, 114 Hz, 126 Hz, and 170 Hz are visible, indicating possible natural frequencies. However, without the use of averaging for Welch's estimate for the correlation function, the frequency content has a high noise floor that limits the prominence of the peaks. In the following, the method of clearing the stabilization diagram is discussed in 4.1.1. Next, the grouping of possible physical modal parameters is walked through in 4.1.2. Finally, the results of assembling the possible physical modes from all roving experiments are presented in 4.1.3.
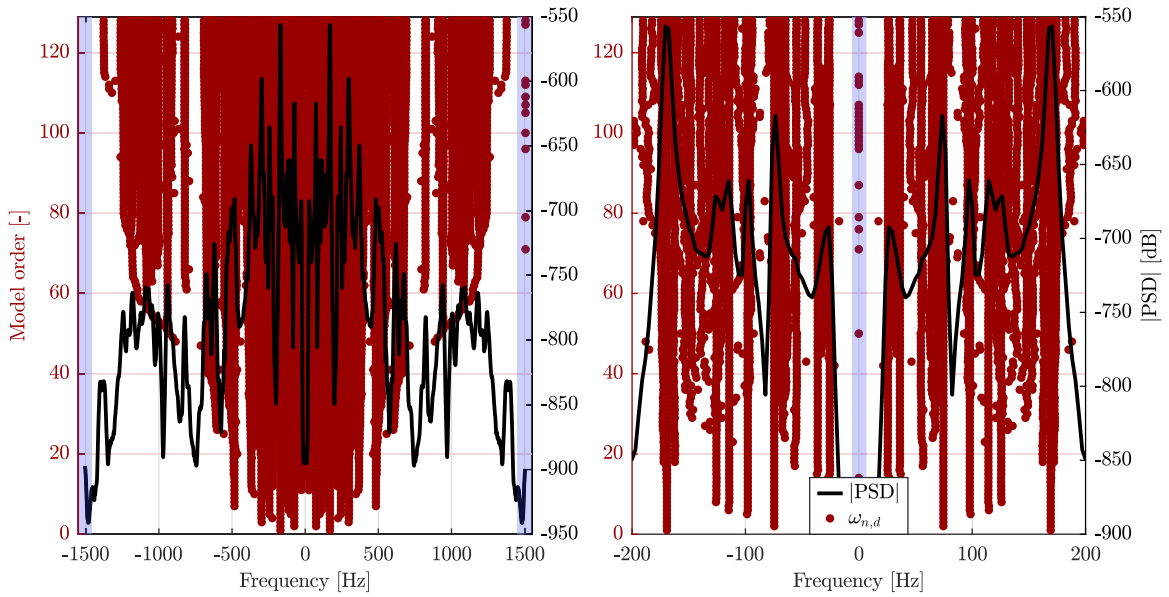
Fig. 6. Presentation of the stabilization diagram for the feature $\omega_{n,d}$ in two frequency ranges for all estimated modes obtained from the SSI method. Blue boxes indicate the regions where modal parameters without a conjugate counterpart lie. (For interpretation of the references to colour in this figure legend, the reader is referred to the web version of this article.)

4.1.1. Clearing the stabilization diagram

The modal parameter estimates obtained from the SSI method using the parameters $s = 256$ and $n_p = 1024$ when incrementing m from 1 to 128 are shown in Fig. 6 as a stabilization diagram for the $\omega_{n,d}$ feature. The full range of the stabilization is presented on the left hand side, while a reduced frequency range is presented on the right. The stabilization diagram presents modal parameters that contain values that do not change much for the $\omega_{n,d}$ feature as vertical lines when the model order is incrementally increased. However, some modal parameters include a clear difference in the estimate of $\omega_{n,d}$ both in the form of singled out dots but also chains that show irregular growth. Some modal parameters estimate a value of 0 Hz or a value of the Nyquist frequency (1506 Hz) for $\omega_{n,d}$ without estimating its complex conjugate counterpart. This is indicated by the blue blocks in Fig. 6. In the figure, the illustration of the negative frequency band serves as a means to check if a modal parameter has a complex conjugate counterpart. In the first case ($\omega_{n,d} = 0$ Hz), the modal parameter characterizes an over-damped mode which the SSI is not built to estimate accurately. In the second case($\omega_{n,d} = 1506$ Hz), the modal parameter estimate is meaningless since it does not describe a mode. The stabilization diagram presents the pool of modal parameters from which an operator, which aims to describe the vibration characteristics of the system manually, can choose from. The graphical presentation of the modal parameters shows the development of the damped natural frequency as a function of an incremental model order. This representation is commonly used since $\omega_{n,d}$ is a feature that quickly stabilizes and easily distinguishes modes. Normally, distance measures that check for the stabilization of one feature at a time are evaluated against a threshold that can be chosen differently for each measure. When the measure is below the threshold, it is said to be stable in that feature. If it is stable in all features, it is said to be a stable mode and, therefore, a candidate to choose as a physical mode. However, for each unique mode, multiple modes will be stable. Therefore, it is different from one operator to another whether a good mode candidate is chosen to represent the vibration characteristics of that mode shape. Another downside of choosing only one stable mode is that information about the vibration kept in other stable modes is neglected.

The distance measures described in 3.3 are calculated for the set of estimated modes presented in the stabilization diagram. The distance measures are used to reduce the number of estimated modes to choose from. The reduction is obtained by a K-means algorithm containing two centroids that either explain possible physical modes or certainly spurious poles. Fig. 7 presents the values of the distance measures and whether an estimated mode with that value of a certain measure is concluded to be part of the first or second centroid. Also, the values of the optimized centroids are illustrated for all different distance measures. The development from the initial to the optimized values of the centroid containing certainly spurious poles is highlighted. The resulting optimized centroid values are [0.004 0.079 0.027 0.079 0.029 0.050 0.102] and [0.049 0.145 0.084 0.150 0.101 0.809 0.958] for the possible physical modes and spurious poles, respectively. On the left in Fig. 7, the distance measures $d\omega_{n,d}$ and $d\zeta$ are presented. The measures illustrate that the defined possible physical modes and spurious poles are difficult to distinguish in these distance measures both by the fact that estimated modes from each group overlap and that the placement of the centroids for the measures lie close. The distance between the centroids in $d\omega_{n,d}$ is 0.045 while it is 0.066 in $d\zeta$. The next illustration shows a similar pattern for the distance measures $d\lambda$ and $dMACX$ as for the measures $d\omega_{n,d}$ and $d\zeta$. The distance measures $d\lambda$ and $dMACX$, therefore, also seem to be unreliable features for distinguishing between possible physical modes and spurious poles as defined by the combination of all distance measures. The third diagram from the left presents the distance measures $dMACX_{\omega_{n,d}}$ and $dMACX_\zeta$. For both measures, estimated modes
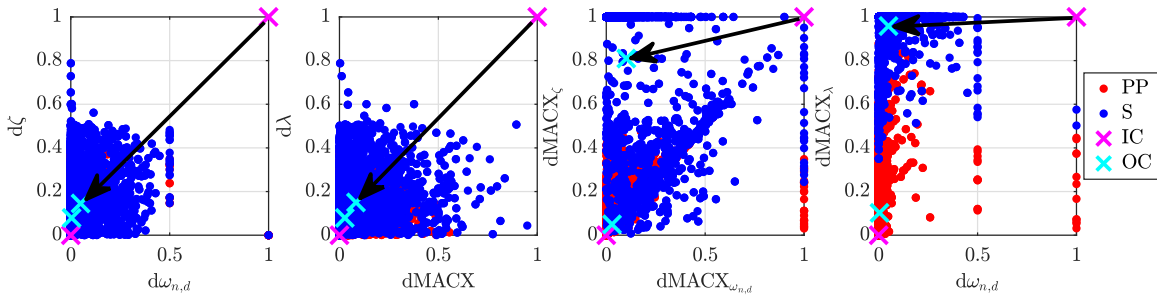
Fig. 7. Presentation of values for distance measures related to the modal parameters of the estimated modes. The value includes an indication of which group of poles the estimated mode belongs to in the K-means optimization algorithm. The two groups are denoted (PP) for possible physical modes and (S) for spurious poles. The development of the coordinates from the initial centroids (IC) to the optimized centroids (OC) is illustrated for the centroids of the group containing spurious poles for each distance measure.

contained in each group overlap. The centroids for the measure $\text{dMACX}_{\omega_{n,d}}$ lie close as was the case for the previously described distance measures. However, for the distance measure dMACX_ζ, the centroids that distinguish between possible physical modes and spurious poles are observed to be separated by a distance of 0.759 between each group. This indicates that this parameter is better suited for dividing the pool of estimated modes into possible physical parameters and spurious poles. An explanation for this must be that the amount of poles that overlap for the distance measure dMACX_ζ is lower than for the other measures. The last diagram in Fig. 7 presents the measures $\text{d}\omega_{n,d}$ and dMACX_λ. The distance measure dMACX_λ presents a limited region for which the estimated modes classified in both groups overlap and the estimated modes are in general well separated between the two classes by this measure. The centroids are separated by a distance of 0.856 in dMACX_λ, making the distance between the centroids that distinguish between possible physical modes and spurious poles the largest for this measure. Additionally, the MACX_λ comparison has been chosen as a parameter that is used to clear the set of estimated modes based on a threshold value of 0.95. The reasons for this choice are that this formulation of the modal assurance criterion contains information about all features of the estimated modal parameters and that this feature can distinguish very well between possible physical modes and certainly spurious poles. The value of the threshold for MACX_λ is decided based on the fact that the parameter is very sensitive to changes in the real part of the eigenvalue which relates to the damping factor. Commonly, and as an example in [33], a 5% change in the damping factor for an estimated mode is chosen as the stabilization threshold for this feature. Therefore, that same threshold is chosen in this work. After the grouping of estimated modes into possible physical modes and spurious poles, the criteria for the damping factor and the eigenvalue are imposed on the set of possible physical modes. If the certainly spurious poles are removed before grouping the modal parameters, a higher risk of wrongly encapsulating possible physical modes in the group of spurious poles will be present.

In Fig. 8, the stability diagram cleared from certainly spurious poles is presented. The diagram in Fig. 8 contains a visibly reduced number of estimated modes when compared to the diagram presented in Fig. 6. Fig. 8 illustrates that no modes without a complex conjugated pole pair exist in the set of modal parameters. Also, it is observed that some of the vertical lines are separated and that more singled out estimated modes are present. Therefore, the next step is to divide the possible physical modes into groups that represent unique physical modes.

4.1.2. Grouping possible physical modes

First, since the possible physical modes are confirmed to include complex conjugated pairs of modal parameters, one mode has its modal parameters conjugated such that no eigenvalues with negative imaginary parts exist. The method used to group the possible physical modes is known as a hierarchical clustering algorithm. The algorithm defines clusters that consist of several possible physical modes. The clusters are defined based on the distance between the possible physical modes. Therefore, a threshold value needs to be defined for the distances between clusters to classify two clusters as different. Multiple methods of evaluating the distances between clusters and potential members of clusters can be defined for the algorithm. The distance measure used to form groups of possible physical modes is chosen as dMACX_λ based on the same reasons for being chosen as an additional threshold measure for grouping between possible physical modes and spurious poles. The threshold is defined as the mean linkage distance used to form the groups when disregarding the linkages between the modal parameters describing the same mode since this is 0. For this experiment, the threshold results in $\text{dMACX}_\lambda = 0.11$. Fig. 9 presents the dendrogram describing the linkage distances between clusters when they are grouped as new branches. A horizontal dashed line indicates the threshold distance between the clusters that is formed at $\text{dMACX}_\lambda = 0.11$. Branches below the threshold are indexed by a colour-marking to illustrate that these belong to the same group of possible physical modes describing a unique physical mode. By the colour-marking it is presented that some unique physical modes are estimated by more possible physical modes in the set of possible physical modes than other unique physical modes. It is claimed that the more possible physical modes that estimate a unique physical mode, the more likely that mode is to be a physical mode. This is a harsh assumption and requires that the modal vector consists of many degrees of freedom to be easily distinguishable. This is one reason to include the measurements of the rotor degrees of freedom in the modal vector.

Based on this claim, the groups are sorted from the group containing the most possible physical modes to the group containing the least amount of possible physical modes. This is illustrated in Fig. 10. A cut-off value is defined for the groups such that if a group
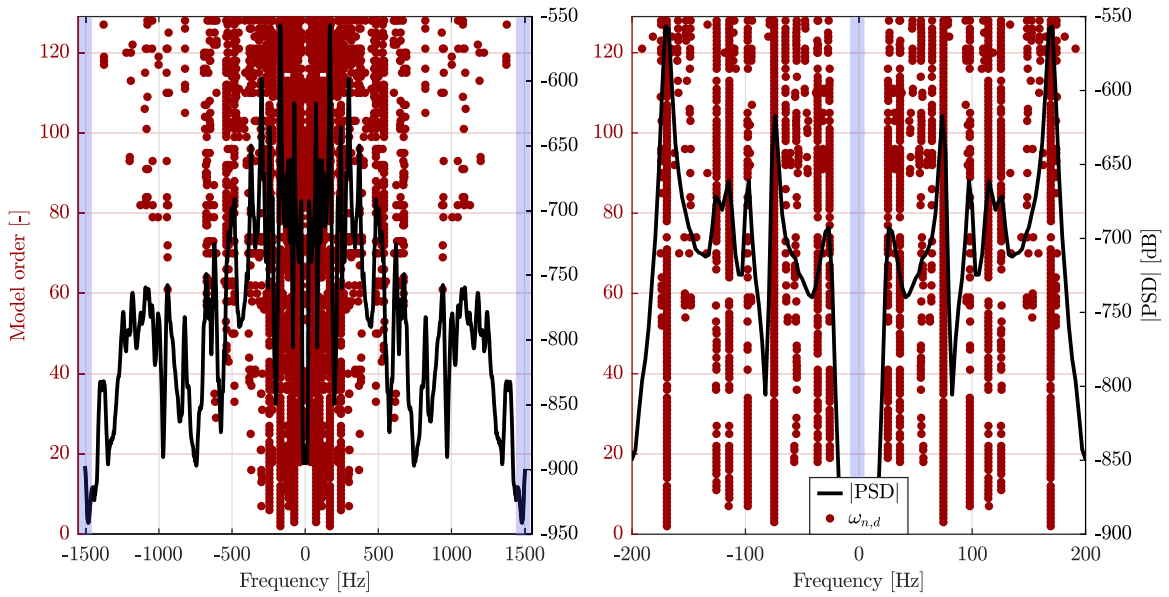
Fig. 8. Presentation of the stabilization diagram for the feature $\omega_{n,d}$ in two frequency ranges for the set of possible physical modes. Blue boxes indicate the regions where modal parameters without a conjugate counterpart lie. (For interpretation of the references to colour in this figure legend, the reader is referred to the web version of this article.)
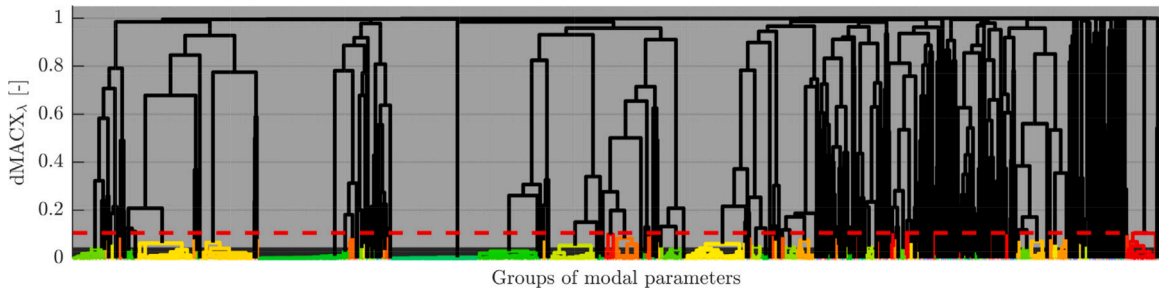

Fig. 9. Dendrogram presenting the distances between the clusters in the hierarchical clustering algorithm including the calculated threshold value used to separate the clusters marked in colour. (For interpretation of the references to colour in this figure legend, the reader is referred to the web version of this article.)

contains less than the mean number of possible physical modes, then that group is regarded as non-physical. The mean number of possible physical modes is the total number of possible physical modes that are clustered divided by the number of clusters. Fig. 10 contains groups marked by blue and red colours. The red coloured groups represent modes with a damped natural frequency of less than 200 Hz, while the blue coloured groups represent modes with a damped natural frequency greater than or equal to 200 Hz. Two cut-off values are presented to illustrate the dependency on the frequency range of interest. If the complete frequency band is considered, the groups containing a minimum of 11 possible physical modes are regarded as unique physical modes. In Fig. 10, 21 groups of possible physical modes with a damped natural frequency less than 200 Hz are above this threshold. Therefore, 21 modes with a damped natural frequency would be regarded as unique physical modes in the frequency band from 0 Hz to 200 Hz. In case only groups containing possible physical modes with a damped natural frequency less than 200 Hz are considered, a cut-off value of 26 possible physical modes is obtained. In this case, Fig. 10 shows that 12 groups of possible physical modes with a damped natural frequency of less than 200 Hz would be regarded as unique physical modes. The reason is suspected to stem from fewer estimated modes in the stabilization diagram with high damped natural frequencies resulting in groups that estimate a high damped natural frequency containing fewer possible physical modes. This will drive down the number of possible physical modes to be contained in a group for that group to be regarded as a representation of a physical mode. No restrictions on the frequency band are imposed for further analysis in this work. Fig. 10 shows that 44 groups of possible physical modes meet the criterion of containing a minimum of 11 possible physical modes in this roving experiment. It does not appear as an unrealistically high number, however, there might be some duplicates of physical modes present based on previous experiences with the specific system being analysed.
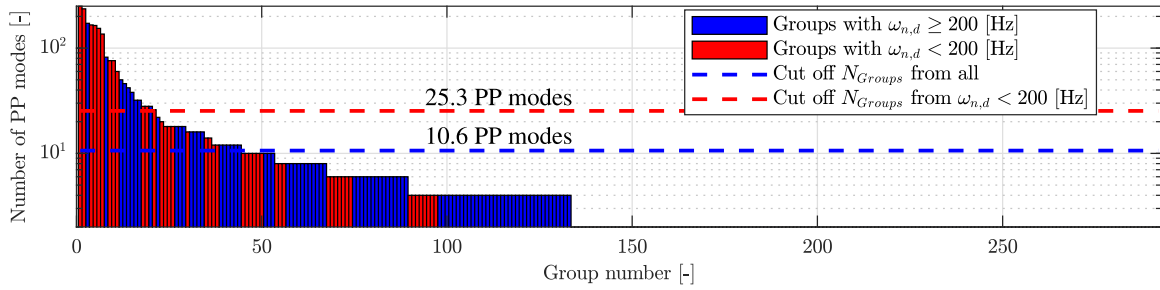
Fig. 10. Histogram of the number of possible physical modes (PP modes) included in each group that describes a mode starting from the group containing the most possible physical modes. If groups contain an equal amount of possible physical modes, the modes are sorted based on the damped natural frequency starting from the lowest. (For interpretation of the references to colour in this figure legend, the reader is referred to the web version of this article.)

4.1.3. Assembling system modes from all roving experiments

As presented in Fig. 3, the unique physical modes from all roving experiments are combined with each roving experiment being the reference in turn resulting in 13 sets of assembled system modes. The sharing of information between the roving experiments, therefore, also contributes to identifying information that is present in multiple experiments, thereby, increasing confidence in which assembled system modes indeed represent a unique system mode. Since this thinking is in line with the reasoning used to group possible physical modes from the cleared stability diagram, the hierarchical clustering and reduction of possible physical modes are used with the same definitions for the thresholds for the assembled system modes describing the complete mode shape of the bed plate structure. The modal parameters of the unique assembled system modes from the combination of all roving experiments are presented in Fig. 11. The unique assembled modes are numbered by the damped natural frequency starting from the unique assembled mode with the lowest damped natural frequency. The modal vector of the bed plate is visualized and the eigenvalue is presented with the mode number. A total of 17 unique assembled modes with a damped natural frequency of less than 200 Hz are identified from the AOMA algorithm. It is observed, that the unique assembled modes do in some cases seem to describe the same physical movement. This could be a symptom of groups with too few assembled modes being regarded as unique assembled modes, thereby, choosing multiple groups that describe a similar system mode.

Therefore, comparisons between the unique assembled modes using the modal assurance criteria MACX and MACX$_\lambda$ are shown in Fig. 12. In the remainder of this paragraph, the unique assembled modes are simply referred to as modes. The comparison through MACX illustrates that the modes 1 and 2, 4 and 5, 5 through 7, 8 through 12, and 13 through 16 could describe the same modes. Another reason for a high comparison through MACX could be found in spatial aliasing. This is illustrated by correlations between modes 1 and 2 and modes 13 through 16 from the MACX in Fig. 12. The comparison through MACX$_\lambda$ presents a lower coupling between the modes. Still, from this comparison couplings between modes 1 and 2, 4 and 5, 6 and 7, 8 and 9, 11 and 12, and 13 through 16 are visible. Since the eigenvalue of mode 5 compared to the eigenvalues of modes 6 and 7 is very different as is the case for modes 8 through 12, these modes compare less using MACX$_\lambda$. It is decided that if modes compare MACX$_\lambda > 0.1$, then these describe the same mode. The modes are grouped until no lower or higher mode compares better than this threshold to any mode in the group. As an example, mode 13 compares MACX$_\lambda = [0.39 \ 0.20 \ 0.16]$ to modes 14 through 16, respectively. The comparisons between mode 12 and modes 13 through 16 are MACX$_\lambda = [6.7 \ 5.4 \ 2.3 \ 4.3] \ 1 \times 10^{-4}$ and between mode 17 and modes 13 through 16 are MACX$_\lambda = [0.27 \ 1.27 \ 0.45 \ 1.85] \ 1 \times 10^{-3}$. Judging from the threshold, it is concluded that modes 13 through 16 are a group of modes that describe the same mode. The visualization of mode 13 also seems sufficiently similar in shape and eigenvalue that it can be concluded to describe the same mode that modes 14 through 16 represent. The comparison of the 17 modes from the AOMA algorithm finds that 9 unique system modes are obtained.

4.2. Comparison to EMA and mathematical model

All modal parameters defined by the AOMA algorithm to describe unique system modes are compared to modal parameters estimated from the EMA experiments and the mathematical model of the test facility. The unique system modes are referred to as chosen physical modes from AOMA in the proceeding. The estimated modes from the EMA experiments and the mathematical model are presented by their damped natural frequency and damping ratio in Table 2. The comparisons focus on chosen physical modes in the frequency range from 0 Hz to 200 Hz and have two objectives. The first objective is to select a unique assembled mode to represent the chosen physical mode for each group of unique assembled modes in the AOMA algorithm which best describes the modal parameters estimated by the EMA experiments and the mathematical model. Secondly, the method evaluates how well the chosen physical modes from the AOMA algorithm compare to the modes estimated from the experiments and the model. Fig. 13 presents the comparisons of the unique assembled modes from the AOMA algorithm to the estimated modes by the EMA experiments and the mathematical model, respectively. The EMA experiments focus on the first ten system modes with vertical movements of the structure. modes 3 and 8 estimated by the EMA algorithm are very uncertain due to a low peak prominence in the frequency signals, violating the assumption for the single degree of freedom peak picking algorithm. The EMA mode comparison shows a good correlation between the remaining eight estimated modes and the unique assembled modes in the AOMA algorithm. The estimated
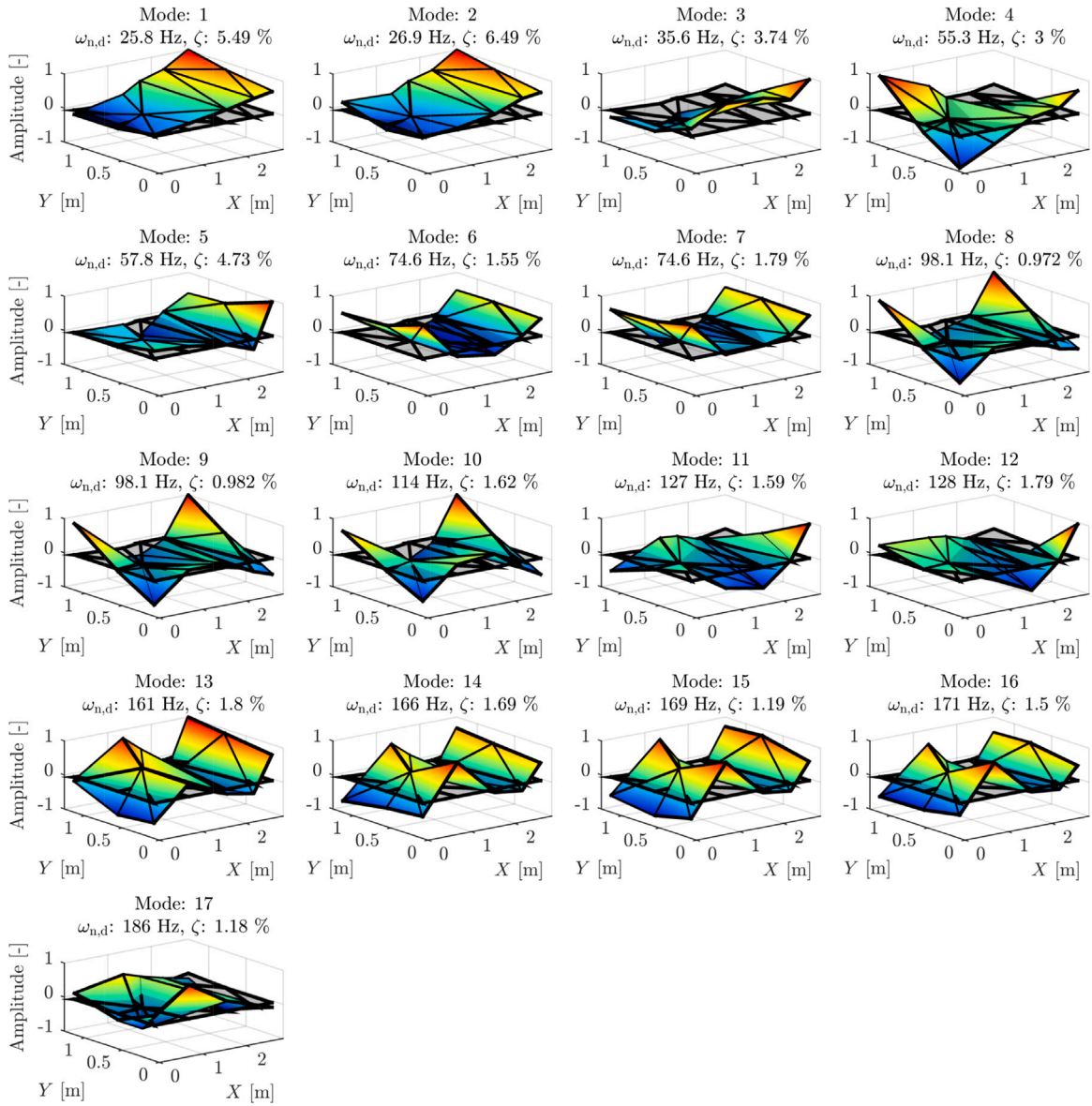
Fig. 11. Unique assembled modes estimated by the AOMA algorithm when the system is influenced by the test conditions **(b)**.

modes from the mathematical model tend to have lower comparability to the unique assembled modes. This comparison shows that the mathematical model estimates an abundance of modes, including the horizontal modes of the bed plate which are out of interest. Therefore, the selection of chosen physical modes from AOMA to compare to the estimated modes from the EMA and the mathematical model also demands choosing the relevant estimated modes. This is done by choosing the unique assembled mode from AOMA that compares best to an estimated mode found in either the EMA experiments or the mathematical model. Using the unique assembled modes 1 and 2 from AOMA as an example, the unique assembled modes compare $\text{MACX}_\lambda = [0.90 \ 0.78]^\text{T}$ to EMA mode 1 and $\text{MACX}_\lambda = [0.69 \ 0.79]^\text{T}$ to mathematical mode 7 as illustrated in Fig. 13. Since unique assembled mode 1 from AOMA compares best to the estimated mode 1 from EMA, unique assembled mode 1 from AOMA is chosen as the representation of mode 1 of the system. Mode 1 of the system compares best to the estimated mode 7 from the mathematical model. Therefore, mode 7 from the mathematical model is compared to the unique assembled mode 1 from AOMA. Using the unique assembled modes 11 and 12 from AOMA as another example, the unique assembled modes 11 and 12 from AOMA are poorly correlated to the modes from the EMA and the mathematical model in Fig. 13. However, the unique assembled mode is still presented.

The best correlated modal parameters of the system obtained via AOMA to the EMA and the mathematical model are presented in Fig. 14. The modal parameters of the chosen physical modes from the AOMA are presented at the top. The modal parameters of the estimated modes from the EMA experiments are presented in the middle and the modal parameters estimated by the mathematical

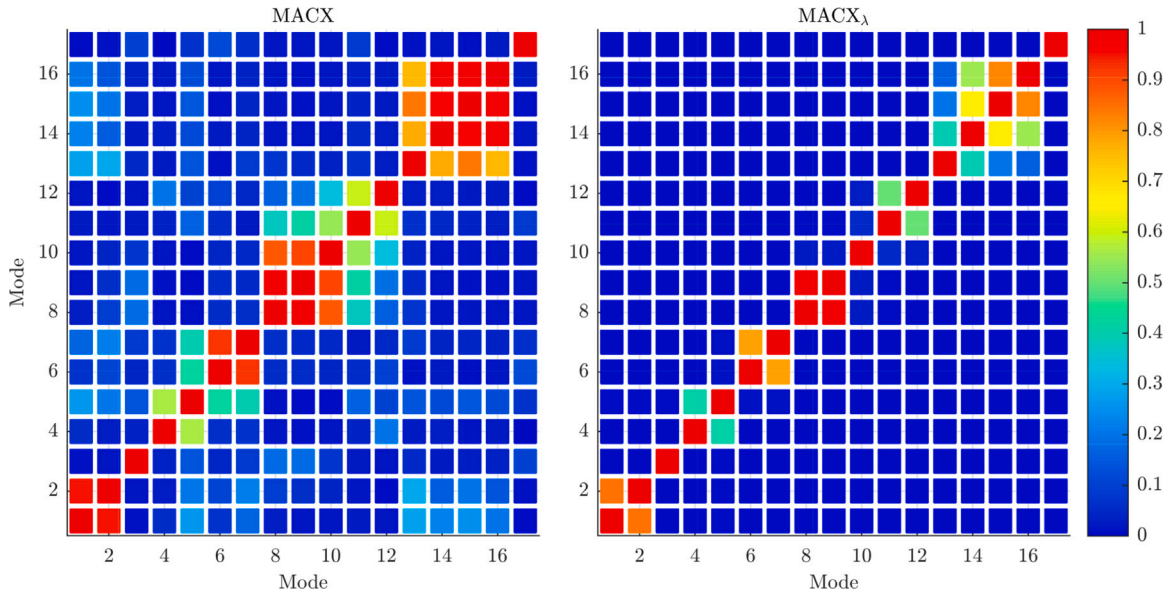**Fig. 12.** Unique assembled modes estimated by the AMOA algorithm compared to each other through MACX and MACX$_\lambda$.

Table 2
Modal parameter estimates from the EMA experiments and the mathematical model of the rotor–foundation system under test conditions **(a)** and **(b)**.

	Mode	1	2	3	4	5	6	7	8	9	10
EMA	$\omega_{n,d}$ [Hz]	25.5	34.9	43.8	56.3	74.1	95.9	114	120	169	190
	ζ [%]	8.67	3.59	14.8	2.31	2.05	0.98	2.00	3.04	0.719	0.902
Math	Mode	1	2	3	4	5	6	7	8	9	10
	$\omega_{n,d}$ [Hz]	0.00	0.059	0.412	16.5	18.8	26.3	27.7	38.5	41.7	56.4
	ζ [%]	100	100	100	4.18	9.08	8.42	10.3	9.18	10.4	12.6
	Mode	11	12	13	14	15	16	17	18	19	
	$\omega_{n,d}$ [Hz]	70.2	72.9	78.0	96.5	97.8	100	110	172	182	
	ζ [%]	50.1	49.3	6.4	29.2	29.6	1.72	4.61	3.04	2.97	

Table 3
Modal parameter estimates of the chosen physical modes from the AOMA algorithm compared to the modal parameter estimates of the modes estimated from the EMA experiments and the mathematical model. The test conditions are described in Table 1, case **(b)**.

	Mode	1	2	3	4	5	6	7	8	9
AOMA	$\omega_{n,d}$ [Hz]	25.8	35.6	55.3	74.6	98.1	114	127	169	186
	ζ [%]	5.49	3.74	3.00	1.55	0.972	1.62	1.59	1.19	1.18
EMA	Mode	1	2	4	5	6	7	8	9	10
	$\omega_{n,d}$ [Hz]	25.5	34.9	56.3	74.1	95.9	114	120	169	190
	$\Delta_{\omega_{n,d}}$ [%]	1.14	1.98	−1.89	0.73	2.24	0.181	5.17	−0.075	−2.14
	ζ [%]	8.67	3.59	2.31	2.05	0.983	1.96	3.04	0.719	0.902
	Δ_ζ [%]	−57.9	4.17	23.0	−32.5	−1.08	−20.7	−91.6	39.8	23.4
	MACX	0.966	0.893	0.926	0.989	0.662	0.939	0.485	0.966	0.658
	MACX$_\lambda$	0.905	0.609	0.754	0.868	0.284	0.920	0.190	0.904	0.309
Math	Mode	7	8	10	13	16	17	17	18	19
	$\omega_{n,d}$ [Hz]	27.7	38.5	56.4	78.0	100	110	110	172	182
	$\Delta_{\omega_{n,d}}$ [%]	−7.41	−8.15	−2.10	−4.54	−2.32	3.66	12.9	−1.59	2.51
	ζ [%]	10.3	9.18	12.6	6.43	1.72	4.61	4.61	3.04	2.97
	Δ_ζ [%]	−88.0	−145	−320	−315	−77.0	−184	−190	−155	−152
	MACX	0.930	0.755	0.888	0.963	0.369	0.954	0.711	0.923	0.400
	MACX$_\lambda$	0.688	0.331	0.480	0.435	0.156	0.547	0.097	0.651	0.227

model are presented at the bottom. If the estimated mode that compares best to the chosen physical mode has a value of MACX$_\lambda \leq 0.1$ then the mode is not presented. The estimated modal parameters from the EMA experiments and the mathematical model are observed to compare very well to all chosen physical modes. Only the chosen physical mode 7 is not observed in the mathematical model.
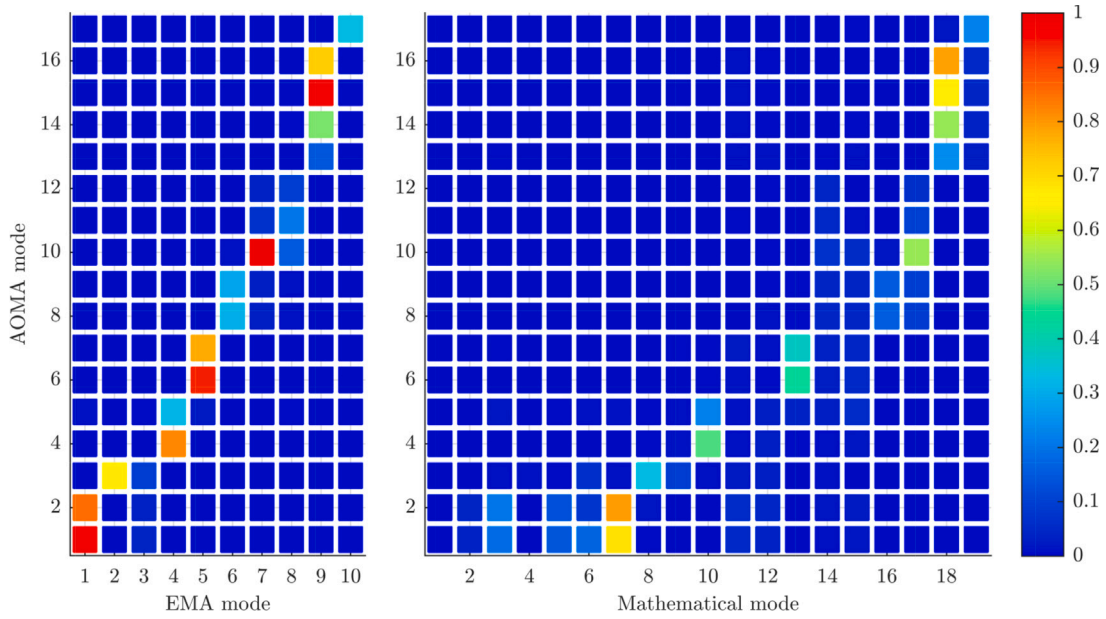
Fig. 13. Unique assembled modes identified from the AOMA algorithm compared to the modes estimated by the EMA and the mathematical model through $MACX_\lambda$.

To quantify how accurately the system modes can be described by the modal parameters estimated from the EMA and the mathematical model, the comparison through $MACX_\lambda$ to the eight modes best estimated from the EMA and all chosen modes n_{Phys} from the mathematical model are summed in Eqs. (14) and (15), respectively. The evaluation of the EMA experiments results in a maximum comparison of 8 if the system modes contain modal parameters that match the modal parameters estimated from the EMA. For the comparison to the mathematical model, a maximum does not exist. In theory, that could result in a wrong interpretation of the comparison between summations of $MACX_\lambda$ if a lot of chosen physical modes are present in the estimation. However, for the tested cases, it is observed that a limited number of system modes are obtained from the analysis. The summations for the EMA experiments and the mathematical model are respectively presented in Eqs. (14) and (15) for test conditions **(b)**.

$$\sum_{i=1}^{8} \max \left(MACX_{\lambda, \mathrm{EMA}, i} \right) \approx \sum [0.90 \;\; 0.61 \;\; 0.75 \;\; 0.87 \;\; 0.28 \;\; 0.92 \;\; 0.90 \;\; 0.31] \approx 5.55 \tag{14}$$

$$\sum_{i=1}^{n_{Phys}} \max \left(MACX_{\lambda, \mathrm{Math}, i} \right) \approx \sum [0.69 \;\; 0.33 \;\; 0.48 \;\; 0.44 \;\; 0.16 \;\; 0.55 \;\; 0.10 \;\; 0.65 \;\; 0.23] \approx 3.61 \tag{15}$$

In this example, the eight modes that compare best to the EMA estimates are [1 2 3 4 5 6 8 9]. The summation of the comparisons between the modal parameters of the chosen physical modes and the EMA estimates results in 5.55 which is high compared to the total of 8. The worst comparing modes are found to be the chosen physical modes 5 and 9. The higher discrepancy is found in the eigenvalue that is least similar for these modes compared to the other modes. The comparison to the mathematical model is 3.61 from a total of 9. It is observed that the modal parameters estimated by the mathematical model in general compare less to the physical modes than the modal parameters from the EMA experiments. This is also found in the eigenvalues that in general estimate a higher damping factor than what is estimated in both the AOMA algorithm and the EMA experiments.

4.3. Dependency of parameters for SSI and operational conditions in seal geometry

The influence of some parameters of the SSI routine on the estimation results is investigated. The parameter intervals are defined to test if settings for the Hankel Matrix can be chosen to reduce the measuring and computational time for a continuous estimation process. It is assumed that a maximum model order of 128 is sufficient to describe relevant system dynamics. The parameters being altered in the analysis are the controls of the Hankel matrix, namely the column height s and the length of the correlation functions n_p. The value of s defines the total amount of singular values that exist for the Hankel matrix. Therefore, the choosing of s also imposes a limitation on the maximum model order m to test for. Table 4 presents the comparison between the modal parameters of the chosen physical modes from the AOMA method and the modal parameters estimated by EMA and the mathematical model. The comparison finds that some values for the parameters used to build the Hankel matrix result in significantly more comparable modal parameters than other values. The use of a column height of $s = 64$ yields very few comparable modal parameters. The reason seems to be that the AOMA algorithm extracts too few physical modes and, thereby, fewer modal parameters to compare
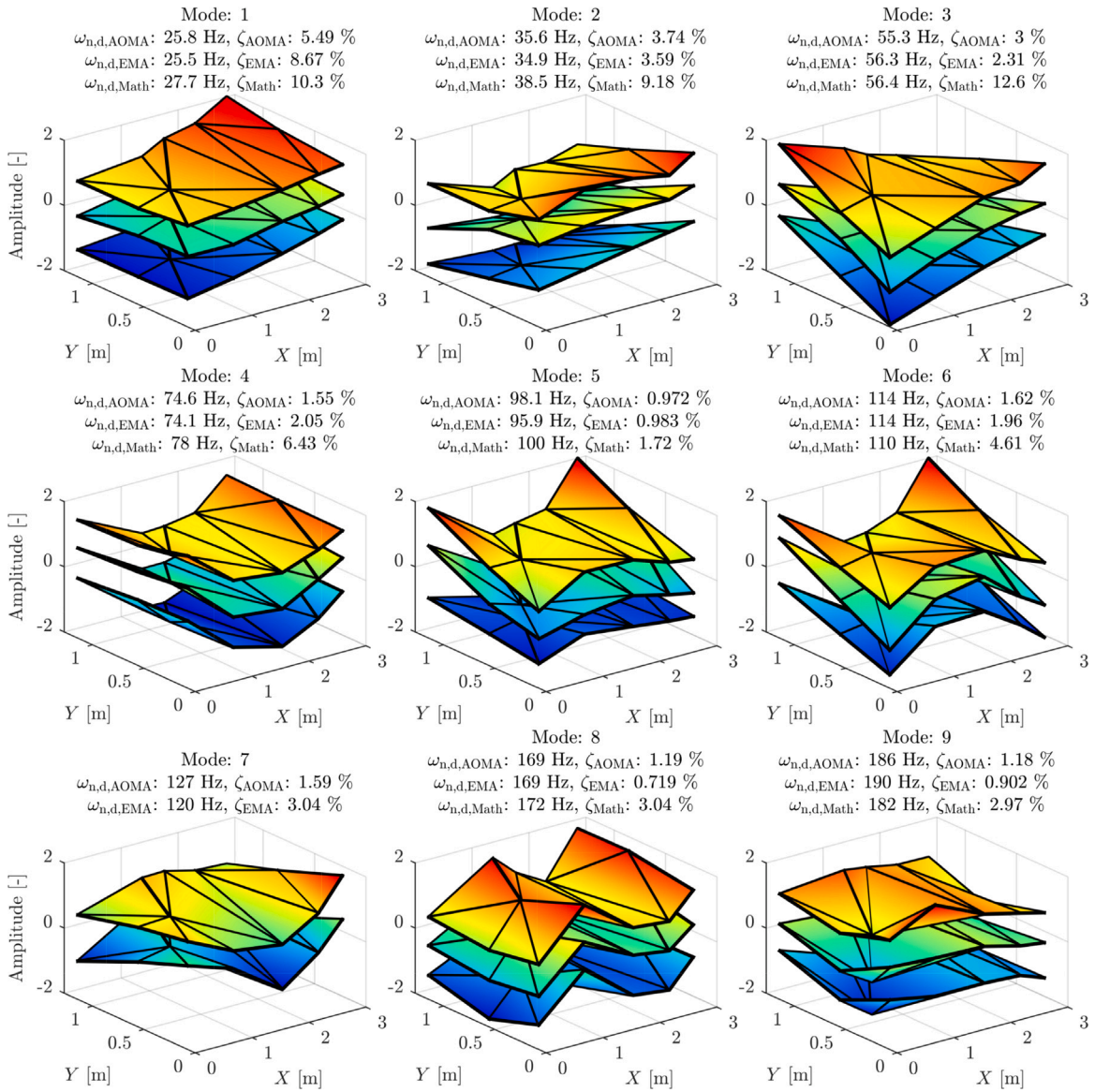
Fig. 14. Chosen physical modes from the AOMA algorithm based on comparisons through $MACX_\lambda$ to the modes estimated from EMA and the mathematical model under test conditions **(b)**. The visualized mode shapes are sorted such that the mode shape from the AOMA algorithm is on top, then the mode shape from EMA is presented below, and furthest down is the mode shape from the mathematical model. If the modes compare $MACX_\lambda \leq 0.1$ then the mode shape is not visualized, as is the case of system mode 7 compared to the mathematical model.

to. This could be a symptom of fewer estimated modes to calculate the physical modes from since the maximum model number is limited to $m = s = 64$. When the column length of the Hankel matrix is increased to the values $s = [128 \ 256 \ 512]$ the modal parameters of the chosen physical modes compare better to the estimated modal parameters. However, this could also stem from the effect of increasing the maximum model parameter. As the column length is further increased to $s = [1024 \ 2048]$, the comparability between the modal parameters drops again. The longer the duration of a signal, the more frequency lines will be distinguishable in the frequency domain of the correlation function. When many frequency lines are present in the frequency domain, low frequency content will be better described. However, this comes at a cost of less data from the total signal to average from, resulting in a greater sensitivity to measurement noise in the signals. Relating this to the Hankel matrix, the column length resembles the block length. Therefore, the longer the columns in the Hankel matrix, the fewer the number of columns to average the estimates from. This means that the noise presented in each column will have a greater impact on the resulting singular values. Another reason to limit the column height is the computational time for the SSI algorithm which grows significantly when increasing s. It has not been tested if the worse comparability with increasing column length can be reduced by increasing the maximum number of m due to high computational times (15 min to 45 min) for each roving experiment for the tests with $s = [1024 \ 2048]$. A dependency in n_p

Table 4

Summation of the comparisons between modal parameters obtained from the AOMA algorithm and modal parameters estimated by EMA and the mathematical model through MACX_λ. The test conditions **(b)** are used.

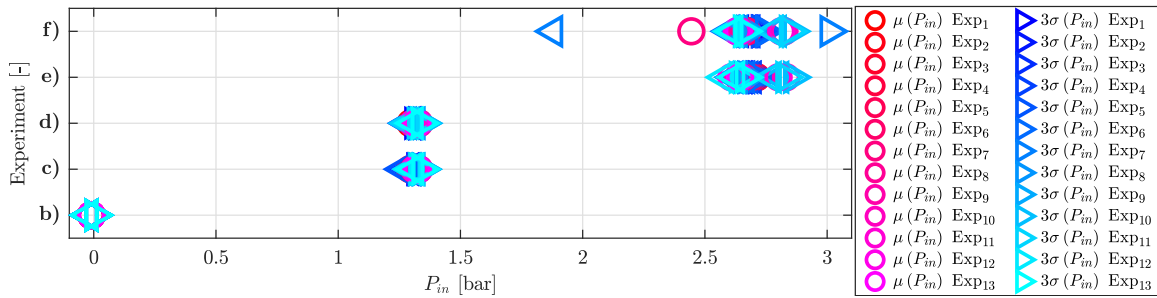|	s	$m\backslash n_p$	256	512	1024	2048	4096	8192	16384
EMA	64	$1 \rightarrow 64$	2.27	2.44	2.13	2.38	2.28	2.21	2.02
	128	$1 \rightarrow 128$	–	4.99	5.26	5.14	4.91	4.68	4.30
	256	$1 \rightarrow 128$	–	–	5.55	5.28	5.37	5.30	5.35
	512	$1 \rightarrow 128$	–	–	–	5.03	4.52	4.23	4.31
	1024	$1 \rightarrow 128$	–	–	–	–	2.88	2.12	1.96
	2048	$1 \rightarrow 128$	–	–	–	–	–	1.33	–
Math	64	$1 \rightarrow 64$	1.57	1.83	1.43	1.70	1.72	1.35	1.26
	128	$1 \rightarrow 128$	–	3.50	3.57	3.66	3.35	3.19	2.85
	256	$1 \rightarrow 128$	–	–	3.61	3.47	3.06	2.92	3.02
	512	$1 \rightarrow 128$	–	–	–	2.49	2.14	2.05	2.17
	1024	$1 \rightarrow 128$	–	–	–	–	1.24	1.26	0.78
	2048	$1 \rightarrow 128$	–	–	–	–	–	0.78	–

Fig. 15. Mean values and standard deviations for the operational conditions of the seal inlet pressure throughout the experimental campaign.

is also present. Since the correlation function is a free decay signal, the longer the delay is extended, the smaller the signal values will be, thereby, adding less information to the singular values. However, more averaging will be possible the longer the correlation function is extended. Therefore, it is expected that an optimum will exist for this parameter as well.

The modal identification tests are repeated for different operational conditions in the seal geometries as described in Table 1. The operational conditions are altered by changing the inlet pressure for the gas entering the seal geometries. For inlet pressures different from 0 bar, the experiments include measurements of the system response when affected by ambient excitations only. The ambient excitations are induced by measurement noise in the sensors for the control algorithms and force disturbances from the turbulent flow in the seal geometries. For all operating points of the seal geometries, one experimental series is carried out with a pseudo random binary signal imposed on the control signals for the current running in the active magnetic bearings of the test facility. Fig. 15 presents the measured inlet pressures for the experiments with imposed noise and ambient excitations only. At high inlet pressures $(\gtrsim 2 \text{ bar})$, the valve used to control the inlet pressure is very sensitive resulting in a greater deviation between each roving experiment. The changes of inlet pressures occur due to a limited amount of gas in a test tank meaning that the tank needs to be refilled multiple times and the inlet pressure reset manually to the desired operational point. For experiment number 7, the pressure in the gas supply tank dropped late in the experiment, resulting in a lower mean inlet pressure and significantly higher standard deviation for the inlet pressure. It is observed that the standard deviation within one experiment in the remainder of the experiments is very small, indicating a precise measurement and pressure regulating system. This also means that deviations in the modes defined as possible physical between the roving experiments are likely to be a result of new operational conditions in that experiment compared to other experiments when a full mode shape is constructed.

The chosen physical modes throughout the experimental campaign are compared to the estimated modes in the EMA experiments and the mathematical model in the same way as in Table 4. The comparisons are summed through all the experiments and presented in Table 5. The comparisons to a great extent present the same trends as Table 4. However, from Table 5, it can be reasoned that the best overall comparison between the chosen physical modes and the estimated modes is obtained by the use of $s = 256$ and $n_p = 1024$. Therefore, the obtained physical modes for all operational conditions both disturbed by ambient disturbances only or also including the imposed noise signal on the control signals are presented in Tables 3 and 6 through Table 9.

The chosen physical modes with an inlet pressure of 1.3 bar identified by the ambient excitations only are presented in Table 6 and Fig. A.1. The calculated possible physical modes are very similar to the ones presented in Fig. 14. Only the modes 7 in both analyses are different. The mode vector of mode shape 7 in Table 6 and Fig. A.1 compares well to the mode vector of mode shape 9. Therefore, it is likely that this mode might be wrongly estimated in the operational conditions of an inlet pressure of 1.3 bar. Additionally, the comparison $\text{MACX}_\lambda \leq 0.1$ between the possible physical mode 5 and the estimated mode 6 is observed from the EMA experiments. Since the possible physical mode still compares to the estimated mathematical mode, this could also be due to the estimation of the mode through EMA.

Table 5

Summation of the summed comparisons between modal parameters obtained from the AOMA algorithm and modal parameters estimated by EMA and the mathematical model through MACX$_\lambda$ for all test conditions in Table 1, cases **(b)** through **(f)**.

	s	$m\backslash n_p$	256	512	1024	2048	4096	8192	16 384
	64	$1 \to 64$	17.0	19.3	17.8	17.8	18.5	17.5	16.6
	128	$1 \to 128$	–	40.6	41.3	38.2	36.7	35.7	32.2
$\sum$(EMA+Math)	256	$1 \to 128$	–	–	41.7	40.7	39.4	39.3	37.2
	512	$1 \to 128$	–	–	–	34.2	30.3	28.9	29.5
	1024	$1 \to 128$	–	–	–	–	21.2	18.1	17.6
	2048	$1 \to 128$	–	–	–	–	–	10.5	–

Table 6

Modal parameter estimates of the chosen physical modes from the AOMA algorithm compared to the modal parameter estimates of the modes estimated from the EMA experiments and the mathematical model. The test conditions are described in Table 1, case **(c)**.

		1	2	3	4	5	6	7	8	9
AOMA	Mode	1	2	3	4	5	6	7	8	9
	$\omega_{n,d}$ [Hz]	25.8	35.4	57.1	74.4	98.6	114	157	169	177
	ζ [%]	2.26	3.19	1.04	1.32	0.855	1.63	0.604	1.19	1.18
EMA	Mode	1	2	4	5	7	7	9	9	10
	$\omega_{n,d}$ [Hz]	24.6	34.7	55.9	74.0	114	114	169	169	190
	$\Delta_{\omega_{n,d}}$ [%]	4.67	2.15	2.13	0.569	−15.8	0.126	−7.87	−0.027	−7.69
	ζ [%]	8.69	4.00	2.08	1.91	1.56	1.56	0.821	0.821	1.02
	Δ_ζ [%]	−284	−25.5	−99.9	−44.9	−83.0	4.03	−35.9	30.9	13.6
	MACX	0.949	0.431	0.925	0.976	0.903	0.958	0.205	0.982	0.718
	MACX$_\lambda$	0.534	0.334	0.541	0.915	0.025	0.952	0.006	0.942	0.056
Math	Mode	10	11	13	15	19	20	22	21	22
	$\omega_{n,d}$ [Hz]	27.7	38.5	56.4	78.0	100	110	182	172	182
	$\Delta_{\omega_{n,d}}$ [%]	−7.05	−8.49	1.24	−4.84	−1.80	3.52	−15.8	−1.56	−2.88
	ζ [%]	10.2	9.25	12.6	6.38	1.72	4.61	2.97	3.08	2.97
	Δ_ζ [%]	−351	−190	−1120	−374	−101	−183	−392	−159	−152
	MACX	0.930	0.633	0.929	0.96	0.367	0.979	0.385	0.900	0.777
	MACX$_\lambda$	0.415	0.287	0.254	0.385	0.181	0.575	0.010	0.628	0.386

Table 7

Modal parameter estimates of the chosen physical modes from the AOMA algorithm compared to the modal parameter estimates of the modes estimated from the EMA experiments and the mathematical model. The test conditions are described in Table 1, case **(d)**.

		1	2	3	4	5	6	7	8	9	10
AOMA	Mode	1	2	3	4	5	6	7	8	9	10
	$\omega_{n,d}$ [Hz]	26.0	32.4	36.1	56.3	74.5	98.2	115	127	169	183
	ζ [%]	4.70	4.95	3.92	5.67	1.39	0.906	1.52	1.85	1.13	0.817
EMA	Mode	1	2	2	4	5	7	7	8	9	10
	$\omega_{n,d}$ [Hz]	24.6	34.7	34.7	55.9	74.0	114	114	121	169	190
	$\Delta_{\omega_{n,d}}$ [%]	5.15	−6.90	4.01	0.659	0.658	−16.3	0.321	4.60	−0.163	−4.05
	ζ [%]	8.69	4.00	4.00	2.08	1.91	1.56	1.56	2.83	0.821	1.02
	Δ_ζ [%]	−85.1	19.3	−2.01	63.4	−37.9	−72.6	−2.67	−52.8	27.2	−24.6
	MACX	0.938	0.272	0.810	0.941	0.982	0.881	0.932	0.605	0.984	0.764
	MACX$_\lambda$	0.746	0.126	0.546	0.702	0.921	0.024	0.903	0.289	0.951	0.130
Math	Mode	10	10	11	13	15	19	20	20	21	22
	$\omega_{n,d}$ [Hz]	27.7	27.7	38.5	56.4	78.0	100	110	110	172	182
	$\Delta_{\omega_{n,d}}$ [%]	−6.50	14.7	−6.42	−0.244	−4.75	−2.30	3.71	13.2	−1.70	0.600
	ζ [%]	10.2	10.2	9.25	12.6	6.38	1.72	4.61	4.61	3.08	2.97
	Δ_ζ [%]	−117	−106	−136	−123	−361	−90.0	−202	−149	−173	−264
	MACX	0.939	0.355	0.887	0.891	0.968	0.363	0.956	0.657	0.920	0.715
	MACX$_\lambda$	0.669	0.115	0.513	0.719	0.409	0.154	0.515	0.099	0.616	0.462

The chosen physical modes with an inlet pressure of 1.3 bar identified by the ambient excitations including the noise signal in the control signals are presented in Table 7 and Fig. A.2. It is observed that 10 different modes are estimated to be present in this analysis. However, possible physical mode 2 compares best to the estimated mode 2 from the EMA experiments and mode 1 in the mathematical model. Therefore, this mode could be estimated due to a matching of modal parameters that describe mode 1 in some roving experiments and mode 2 in other roving experiments. The choosing of this exact mode is what ideally should be avoided from the hierarchical clustering algorithm. The remainder of the calculated possible physical modes are very similar to the ones presented in Fig. 14. It is also observed that the comparison MACX$_\lambda \leq 0.1$ between the possible physical mode 6 and the estimated mode 6 from the EMA experiments exists for this analysis as well, further indicating that the low comparison to this chosen mode is due to the estimation of the mode through EMA.

The chosen physical modes with an inlet pressure of 2.7 bar identified by the ambient excitations only are presented in Table 8 and Fig. A.3. The AOMA algorithm finds 7 possible physical modes for this operational condition when the identification is carried out with the ambient excitations from the turbulent flow in the seal geometries. Mode 1 seems to have some points in the mode

Table 8

Modal parameter estimates of the chosen physical modes from the AOMA algorithm compared to the modal parameter estimates of the modes estimated from the EMA experiments and the mathematical model. The test conditions are described in Table 1, case **(e)**.

	Mode	1	2	3	4	5	6	7
AOMA	$\omega_{n,d}$ [Hz]	26.6	35.3	56.7	75.0	98.2	115	169
	ζ [%]	4.38	5.53	1.93	1.91	0.825	1.89	1.24
	Mode	1	2	4	5	7	7	9
	$\omega_{n,d}$ [Hz]	25.1	34.9	55.8	74.1	114	114	169
	$\Delta_{\omega_{n,d}}$ [%]	5.57	1.18	1.64	1.21	−16.5	0.355	0.105
EMA	ζ [%]	9.53	2.88	1.92	1.92	2.42	2.42	0.874
	Δ_{ζ} [%]	−118	47.9	0.094	7.31	−193	−28.1	29.7
	MACX	0.454	0.658	0.949	0.962	0.799	0.925	0.939
	MACX$_\lambda$	0.330	0.424	0.795	0.862	0.029	0.902	0.902
	Mode	9	10	14	15	19	20	21
	$\omega_{n,d}$ [Hz]	27.7	38.1	56.5	78.0	100	110	172
	$\Delta_{\omega_{n,d}}$ [%]	−4.24	−7.76	0.375	−4.07	−2.27	3.94	−1.56
Math	ζ [%]	9.08	8.82	12.7	6.24	1.72	4.61	3.11
	Δ_{ζ} [%]	−107	−59.5	−558	−226	−109	−144	−150
	MACX	0.474	0.851	0.948	0.971	0.342	0.984	0.922
	MACX$_\lambda$	0.363	0.463	0.428	0.554	0.130	0.593	0.658

Table 9

Modal parameter estimates of the chosen physical modes from the AOMA algorithm compared to the modal parameter estimates of the modes estimated from the EMA experiments and the mathematical model. The test conditions are described in Table 1, case **(f)**.

	Mode	1	2	3	4	5	6	7	8	9
AOMA	$\omega_{n,d}$ [Hz]	26.1	36.2	40.2	56.5	73.9	97.7	115	139	169
	ζ [%]	5.91	2.88	6.93	3.72	1.69	0.971	1.50	2.34	1.15
	Mode	1	2	2	4	5	7	7	9	9
	$\omega_{n,d}$ [Hz]	25.1	34.9	34.9	55.8	74.1	114	114	169	169
	$\Delta_{\omega_{n,d}}$ [%]	3.74	3.48	13.1	1.25	−0.247	−17.1	0.241	−21.8	0.126
EMA	ζ [%]	9.53	2.88	2.88	1.92	1.77	2.42	2.42	0.873	0.873
	Δ_{ζ} [%]	−61.3	−0.201	58.4	48.3	−5.12	−149	−61.3	62.7	23.8
	MACX	0.878	0.890	0.083	0.917	0.979	0.821	0.870	0.233	0.953
	MACX$_\lambda$	0.774	0.569	0.022	0.778	0.968	0.033	0.764	0.005	0.929
	Mode	9	10	12	14	15	19	20	18	21
	$\omega_{n,d}$ [Hz]	27.7	38.1	42.5	56.5	78.0	100	110	97.7	172
	$\Delta_{\omega_{n,d}}$ [%]	−6.26	−5.25	−5.80	−0.022	−5.61	−2.80	3.83	29.6	−1.54
Math	ζ [%]	9.08	8.82	24.1	12.7	6.24	1.72	4.61	30.3	3.11
	Δ_{ζ} [%]	−53.6	−207	−248	−240	−269	−77.3	−208	−1120	−171
	MACX	0.845	0.915	0.430	0.917	0.957	0.364	0.915	0.337	0.920
	MACX$_\lambda$	0.673	0.521	0.256	0.627	0.430	0.134	0.454	0.036	0.635

Table 10

Total comparison of the modal parameters obtained from the AOMA algorithms to the modal parameters estimated by the EMA experiments and mathematical model through MACX$_\lambda$ with $s = 256$ when changing the initial delay τ_1 for the correlation functions. The test conditions in Table 1, case **(b)**, are used.

	τ_1	$m \backslash n_p$	1024	2048	4096	8192	16 384
	0	$1 \to 128$	5.55	5.28	5.37	5.30	5.35
	1	$1 \to 128$	5.37	5.28	5.38	5.22	5.31
	2	$1 \to 128$	5.34	5.34	5.29	5.58	5.35
EMA	3	$1 \to 128$	4.98	5.25	5.25	5.35	5.17
	10	$1 \to 128$	5.34	5.32	4.84	5.34	5.16
	20	$1 \to 128$	5.23	5.17	5.14	5.31	5.39
	30	$1 \to 128$	4.81	5.29	5.00	5.38	5.25
	0	$1 \to 128$	3.61	3.47	3.06	2.92	3.02
	1	$1 \to 128$	3.66	3.43	3.07	2.80	2.99
	2	$1 \to 128$	3.62	3.41	3.12	3.21	3.07
Math	3	$1 \to 128$	3.53	3.22	3.02	2.97	3.03
	10	$1 \to 128$	3.55	3.45	2.71	3.05	3.03
	20	$1 \to 128$	3.60	3.56	2.90	3.23	3.20
	30	$1 \to 128$	3.42	3.20	2.96	3.12	3.03

vector which are phase shifted compared to the other points. Comparing these modes to the modes in Fig. 14, it is noticed that the chosen physical modes 7 and 9 are not identified in Fig. A.3. This could be a result of the frequency content of the ambient excitations either not being as broad band as necessary for this operational condition or changes to the system from the operational
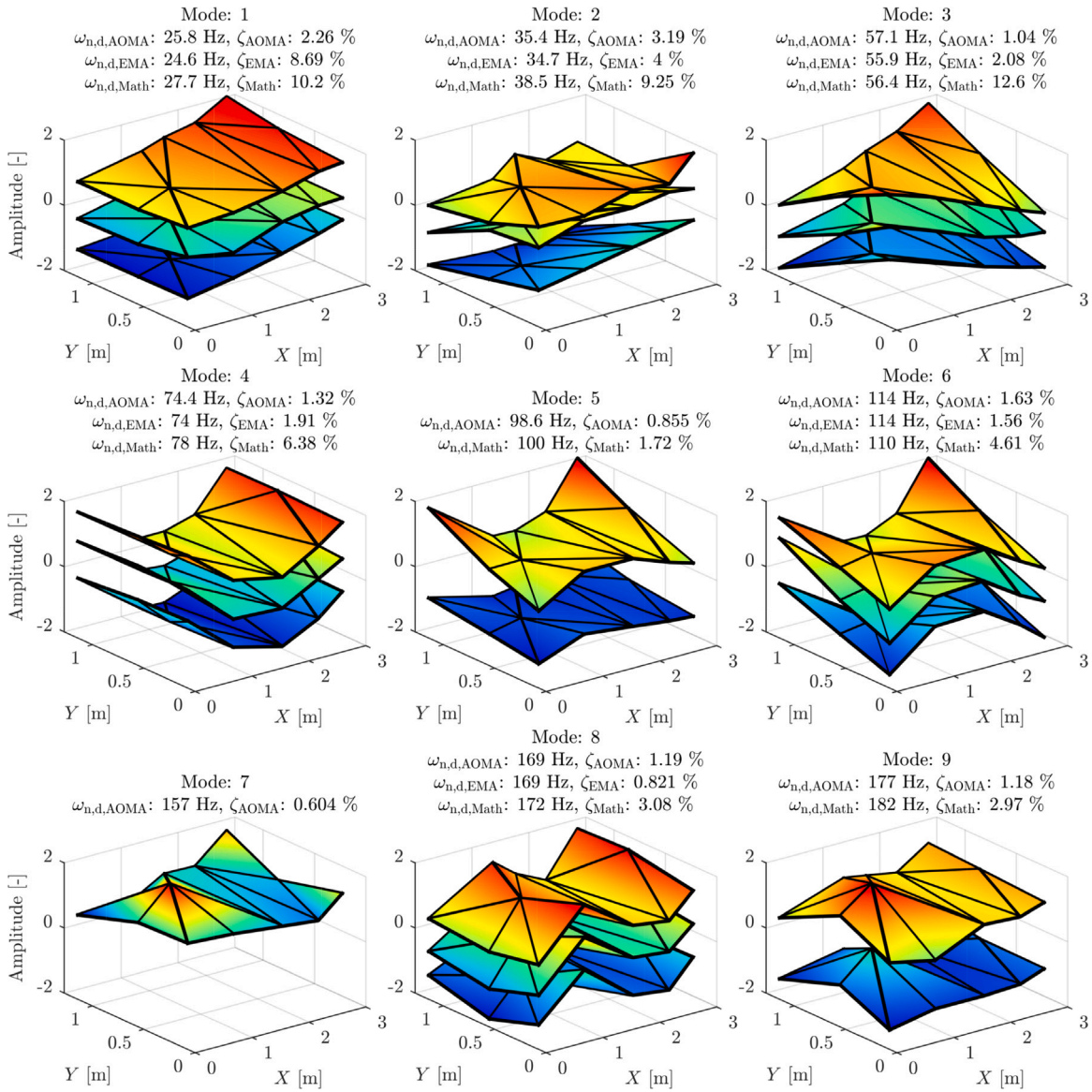
Fig. A.1. Chosen physical modes from the AOMA algorithm based on comparisons through MACX_λ to the modes estimated from EMA and the mathematical model under test conditions **(c)**. The visualized mode shapes are sorted such that the mode shape from the AOMA algorithm is on top, then the mode shape from EMA is presented below, and furthest down is the mode shape from the mathematical model. If the modes compare $\text{MACX}_\lambda \leq 0.1$ then the mode shape is not visualized.

conditions making the modes less pronounced in the response. Again, for this identification, the comparison $\text{MACX}_\lambda \leq 0.1$ between the possible physical mode 5 and the estimated mode 6 is observed from the EMA experiments.

The chosen physical modes with an inlet pressure of 2.7 bar identified by the ambient excitations including the noise signal in the control signals are presented in Table 9 and Fig. A.4. Nine different physical modes have been selected, however, modes 3 and 8 have not been identified previously. Mode 3 is well described by the mathematical model. This means that this mode could have increased its prominence in the response due to changes in the operational conditions or by the combination of higher ambient disturbances in combination with the noisy signal in the control signals of the active magnetic bearings. Mode 8 looks like a combination between the chosen modes 7 and 9. Since this mode is not estimated in any of the other identifications, it is concluded to be a falsely identified mode. This means that neither the chosen physical modes 7 nor 9 identified in Fig. 14 are identified for the operational conditions in the seal geometry dictated by an inlet pressure of 2.7 bar by the AOMA algorithm. This backs up the suspicion that the operational conditions have reduced the prominence of these modes in the output responses.

When working with white noise signals in a correlation function, a time delay of 0 will result in a correlation of unity and 0 when the time delay is increased to 1 sample. The assumption of a white noise disturbance could therefore influence the resulting
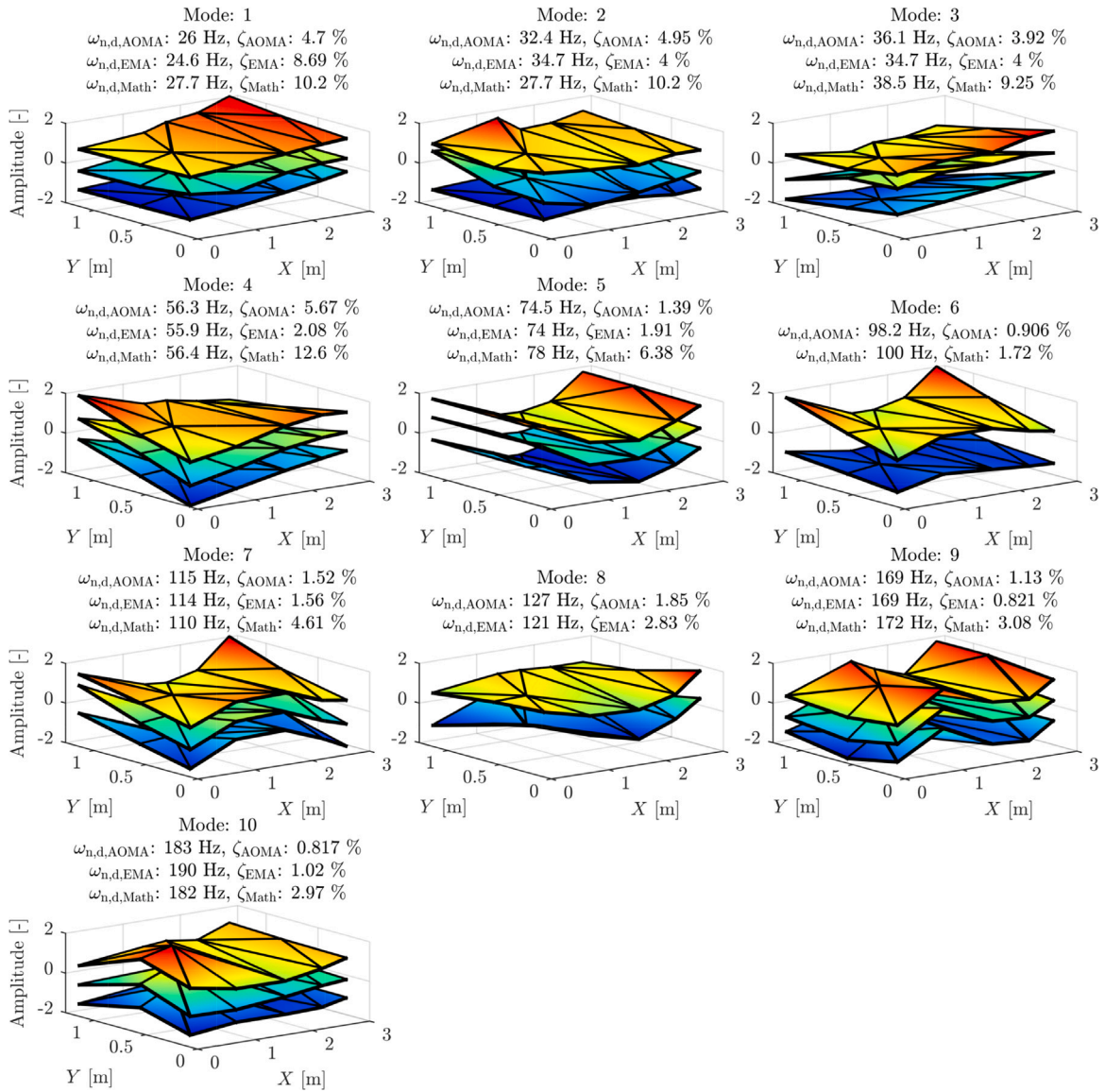
Fig. A.2. Chosen physical modes from the AOMA algorithm based on comparisons through MACX_λ to the modes estimated from EMA and the mathematical model under test conditions **(d)**. The visualized mode shapes are sorted such that the mode shape from the AOMA algorithm is on top, then the mode shape from EMA is presented below, and furthest down is the mode shape from the mathematical model. If the modes compare $\text{MACX}_\lambda \leq 0.1$ then the mode shape is not visualized.

correlation function depending on the chosen initial time delay [34]. Therefore, a short study on the use of the initial delay for the correlation function is presented in Table 10. The analysis finds that the initial delay does affect the resulting comparability of the modal parameters describing the chosen physical modes. However, the values of the comparisons do not seem to converge to a specific number as presented in [34]. This could be due to changes in many stages of the AOMA algorithm from a change in the initial delay of the correlation function. One explanation could be that the analysis of the roving experiments is differently impacted by a change to the initial delay of the correlation function resulting in fluctuations in the measurements for a higher number of samplings for the initial delay than presented in [34].

5. Conclusions

The article presents an analysis of vibration characteristics for a supporting structure of a rotating machine. The analysis is carried out using an automated modal parameter identification algorithm that relies on modal parameters sorted in a stabilization diagram. Since the analysis is carried out in the framework of OMA using a limited amount of sensors, it is expanded to combine information from multiple roving experiments.
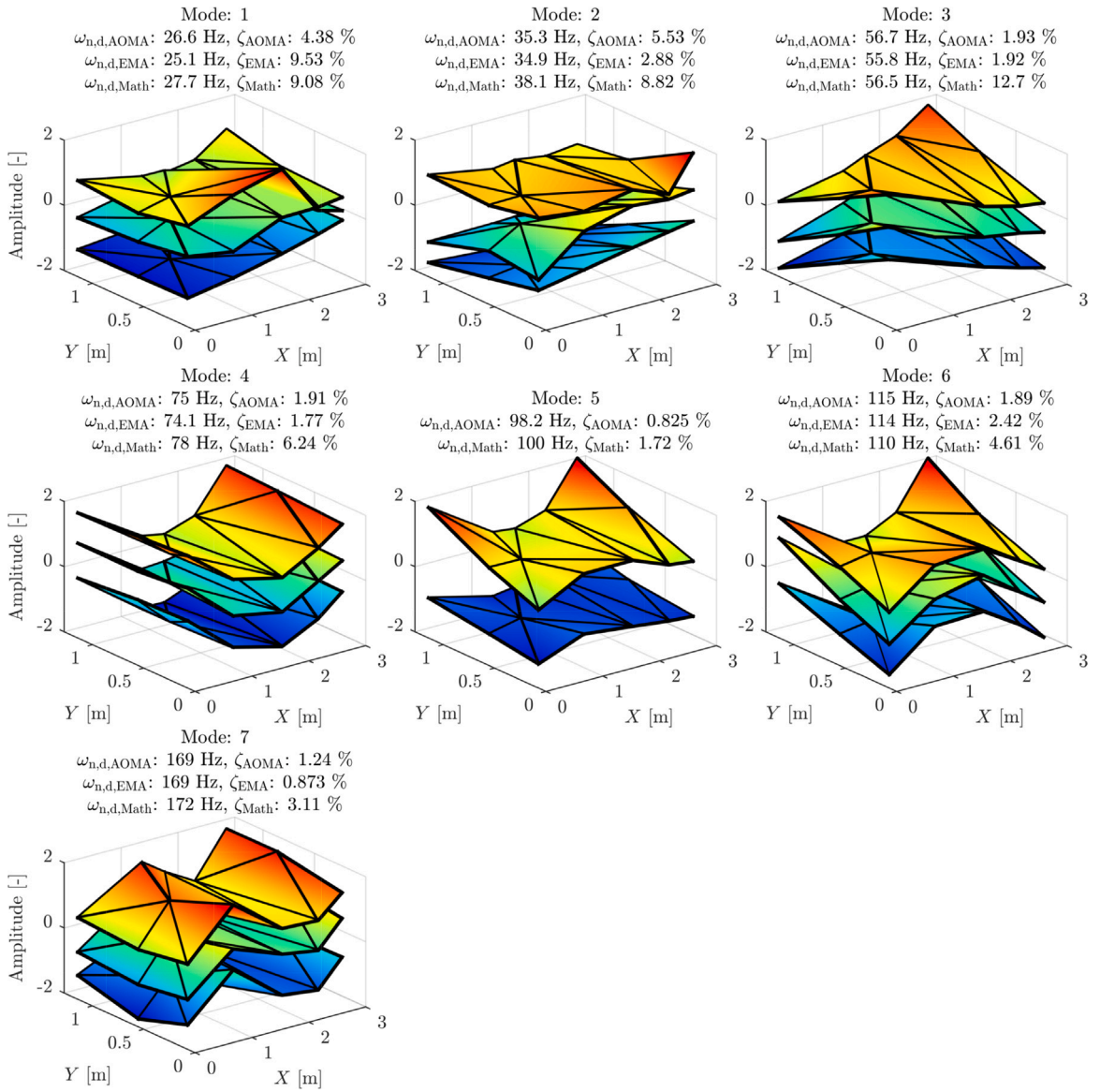
Fig. A.3. Chosen physical modes from the AOMA algorithm based on comparisons through MACX_λ to the modes estimated from EMA and the mathematical model under test conditions **(e)**. The visualized mode shapes are sorted such that the mode shape from the AOMA algorithm is on top, then the mode shape from EMA is presented below, and furthest down is the mode shape from the mathematical model. If the modes compare $\text{MACX}_\lambda \leq 0.1$ then the mode shape is not visualized.

Intermediate results from the automated modal parameter identification algorithm present that when a K-means algorithm is used for clearing a stabilization diagram, some distance measures perform better than others in distinguishing between possible physical and certainly spurious poles. For the tested distance measures, only two measures show a very distant mean value between the two groups, namely dMACX_ζ and dMACX_λ. Since, the dMACX_λ distance measure shows the least overlapping between the groups, a threshold for this measure is chosen to distinguish the estimated parameters between possible physical modes and certainly spurious poles.

In the hierarchical clustering algorithm, a threshold is used for the number of estimated modes contained in a group for that group to be considered as a representation of a possible physical mode. It is presented that the threshold depends on the frequency band assumed for the system. If a wide frequency band is considered, it is presented that groups containing few estimated modes might be chosen as possible physical modes even though a similar mode is present in another group. However, a more correct way is to impose a frequency band directly on the estimation method to limit the frequency content to be considered.
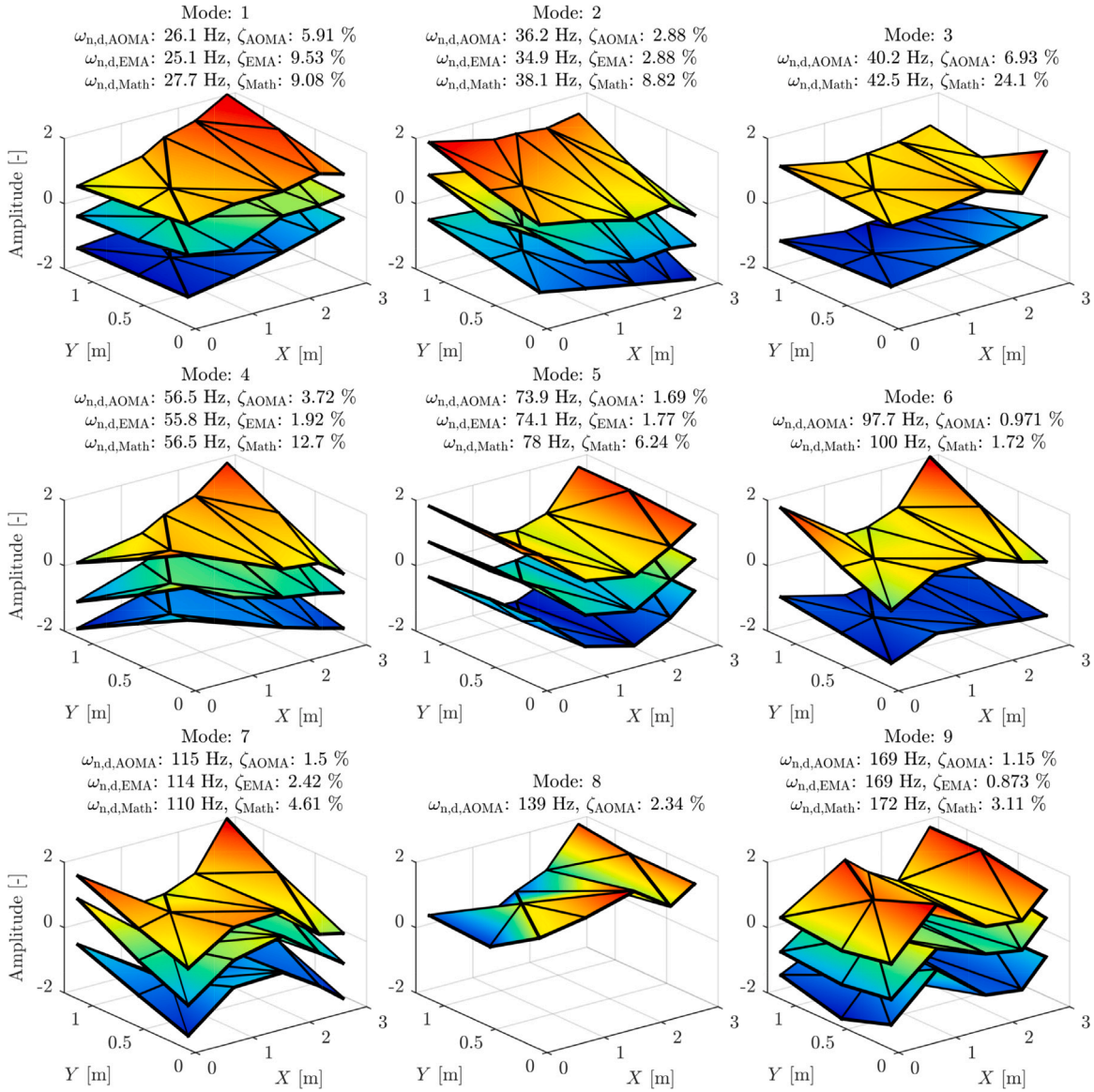
Fig. A.4. Chosen physical modes from the AOMA algorithm based on comparisons through MACX$_\lambda$ to the modes estimated from EMA and the mathematical model under test conditions **(f)**. The visualized mode shapes are sorted such that the mode shape from the AOMA algorithm is on top, then the mode shape from EMA is presented below, and furthest down is the mode shape from the mathematical model. If the modes compare MACX$_\lambda \leq 0.1$ then the mode shape is not visualized.

The modes extracted from the automated modal parameter identification algorithm do for some modes present similar vibration characteristics. In this work, comparisons through MACX$_\lambda$ between the modes are used to evaluate the similarity. If modes are deemed similar, a comparison to other estimation methods is used to determine which physical modes of the similar ones to choose.

The identification algorithm is tested for multiple operational conditions in two seals mounted in a back-to-back configuration for two types of disturbances. The chosen physical modes are for each tested configuration able to describe at least seven modes of the bed plate identified from either EMA tests or a mathematical model of the test facility. This means that the ambient disturbance present in the seals due to turbulent gas flow is sufficient as excitation to the rotor–foundation system to be used as a way to identify the vibration characteristics in the system. It also means that the automated modal parameter identification algorithm is reliable with regard to the estimated physical modes that the algorithm produces.

CRediT authorship contribution statement

Thomas T. Paulsen: Writing – review & editing, Writing – original draft, Visualization, Validation, Project administration, Methodology, Investigation, Conceptualization. **Sebastian V. Damsgaard:** Writing – review & editing, Validation, Investigation, Data curation. **Ilmar F. Santos:** Writing – review & editing, Supervision, Project administration, Methodology.

Declaration of competing interest

The authors declare that they have no known competing financial interests or personal relationships that could have appeared to influence the work reported in this paper.

Data availability

Data will be made available on request.

Appendix A. Visual modal parameter comparisons of chosen physical modes to estimated modes from the EMA and the mathematical model

See Figs. A.1–A.4.

References

[1] B.J. Schwarz, M.H. Richardson, Experimental modal analysis, CSI Reliab. Week 35 (1) (1999) 1–12, URL http://papers.vibetech.com/Paper28-ExperimentalModalAnalysis.pdf.
[2] Y. Bidaut, U. Baumann, S.M.H. Al-Harthy, et al., Rotordynamic stability of a 9500 psi reinjection centrifugal compressor equipped with a hole pattern seal-measurement versus prediction taking into account the operational boundary conditions., in: Proceedings of the 38th Turbomachinery Symposium, Texas A&M University. Turbomachinery Laboratories, 2009.
[3] R. Brincker, C. Ventura, Introduction to Operational Modal Analysis, John Wiley & Sons, 2015.
[4] E. Reynders, System identification methods for (operational) modal analysis: review and comparison, Arch. Comput. Methods Eng. 19 (1) (2012) 51–124.
[5] E. Lazzarini, G. Frison, D. Trutalli, L. Marchi, R. Scotta, Comfort assessment of high-rise timber buildings exposed to wind-induced vibrations, Struct. Des. Tall Special Build. 30 (12) (2021) e1882, http://dx.doi.org/10.1002/tal.1882.
[6] L. Hermans, H. Van der Auweraer, Modal testing and analysis of structures under operational conditions: industrial applications, Mech. Syst. Signal Process. 13 (2) (1999) 193–216.
[7] F. Magalhães, Á. Cunha, Explaining operational modal analysis with data from an arch bridge, Mech. Syst. Signal Process. 25 (5) (2011) 1431–1450, http://dx.doi.org/10.1016/j.ymssp.2010.08.00.
[8] E. Reynders, Uncertainty quantification in data-driven stochastic subspace identification, Arch. Comput. Methods Eng. 19 (2021) 107338, http://dx.doi.org/10.1016/j.ymssp.2020.107338.
[9] L.B. Saint Martin, L.L. Gusmão, T.H. Machado, E.P. Okabe, K.L. Cavalca, Operational modal analysis application to support structure identification under rotating machinery unbalance, Eng. Struct. 249 (2021) 113344, http://dx.doi.org/10.1016/j.engstruct.2021.113344.
[10] C.R. Farrar, K. Worden, An introduction to structural health monitoring, Phil. Trans. R. Soc. A 365 (1851) (2007) 303–315.
[11] A. Davies, Handbook of Condition Monitoring: Techniques and Methodology, Springer Science & Business Media, 1998.
[12] M. Tiboni, C. Remino, R. Bussola, C. Amici, A review on vibration-based condition monitoring of rotating machinery, Appl. Sci. 12 (3) (2022) 972, http://dx.doi.org/10.3390/app12030972.
[13] F. Magalhães, Á. Cunha, E. Caetano, Online automatic identification of the modal parameters of a long span arch bridge, Mech. Syst. Signal Process. 23 (2) (2009) 316–329, http://dx.doi.org/10.1016/j.ymssp.2008.05.003.
[14] E. Reynders, J. Houbrechts, G. De Roeck, Fully automated (operational) modal analysis, Mech. Syst. Signal Process. 29 (2012) 228–250, http://dx.doi.org/10.1016/j.ymssp.2012.01.007.
[15] E. Neu, F. Janser, A.A. Khatibi, A.C. Orifici, Fully automated operational modal analysis using multi-stage clustering, Mech. Syst. Signal Process. 84 (2017) 308–323.
[16] P.E. Charbonnel, Fuzzy-driven strategy for fully automated modal analysis: Application to the SMART2013 shaking-table test campaign, Mech. Syst. Signal Process. 152 (2021) 107388.
[17] V. Mugnaini, L.Z. Fragonara, M. Civera, A machine learning approach for automatic operational modal analysis, Mech. Syst. Signal Process. 170 (2022) 108813.
[18] E. Tronci, M. De Angelis, R. Betti, V. Altomare, Multi-stage semi-automated methodology for modal parameters estimation adopting parametric system identification algorithms, Mech. Syst. Signal Process. 165 (2022) 108317.
[19] J.V. Covioli, G. Coppotelli, On the use of Gaussian mixture models for automated modal parameters estimation, in: AIAA Scitech 2021 Forum, 2021, p. 1035.
[20] J. Zeng, Z. Hu, Automated operational modal analysis using variational Gaussian mixture model, Eng. Struct. 273 (2022) 115139, http://dx.doi.org/10.1016/j.engstruct.2022.115139.
[21] J. Priou, S. Gres, M. Perrault, L. Guerineau, M. Döhler, Automated uncertainty-based extraction of modal parameters from stabilization diagrams, in: IOMAC 2022-9th International Operational Modal Analysis Conference, 2022, URL https://hal.inria.fr/hal-03722921/document.
[22] P. Mellinger, M. Döhler, L. Mevel, Variance estimation of modal parameters from output-only and input/output subspace-based system identification, J. Sound Vib. 379 (2016) 1–27, http://dx.doi.org/10.1016/j.jsv.2016.05.037.
[23] S. Greś, M. Döhler, L. Mevel, Uncertainty quantification of the Modal Assurance Criterion in operational modal analysis, Mech. Syst. Signal Process. 152 (2021) 107457, http://dx.doi.org/10.1016/j.ymssp.2020.107457.
[24] T.T. Paulsen, G. Coppotelli, I.F. Santos, On the Accuracy of Modal Parameter Estimates in Operational Modal Analysis considering Boundary Conditions [Manuscript submitted for publication, MSSP23-4145], Department of Civil and Mechanical Engineering, Technical University of Denmark, 2022.
[25] T.T. Paulsen, I.F. Santos, L.K.H. Clemmensen, Contribution to the estimation of force coefficients of plain gas seals with high preswirl considering rotor-foundation dynamics, Mech. Syst. Signal Process. 186 (2023) 109885, http://dx.doi.org/10.1016/j.ymssp.2022.109885.

[26] A.J. Voigt, C. Mandrup-Poulsen, K. Nielsen, I. Santos, Design and calibration of a full-scale active magnetic bearing-based test facility for investigating rotordynamic properties of turbomachinery seals in multiphase flow, J. Eng. Gas Turb. Power 139 (5) (2017) 052505, http://dx.doi.org/10.1115/1.4035176.

[27] P. Welch, The use of fast Fourier transform for the estimation of power spectra: a method based on time averaging over short, modified periodograms, IEEE Trans. Audio Electroacoustics 15 (2) (1967) 70–73.

[28] H. Vold, J. Crowley, G.T. Rocklin, New ways of estimating frequency response functions, Sound Vibr. 18 (11) (1984) 34–38.

[29] D.J. Ewins, Modal Testing: Theory, Practice and Application, Wiley, 2000.

[30] D.L. Brown, R.J. Allemang, R. Zimmerman, M. Mergeay, Parameter estimation techniques for modal analysis, SAE Trans. (1979) 828–846.

[31] P. Van Overschee, B. De Moor, Subspace Identification for Linear Systems: Theory Implementation Applications, Kluwer Academic Publishers, 1996.

[32] P. Vacher, B. Jacquier, A. Bucharles, Extensions of the MAC criterion to complex modes, in: Proceedings of the International Conference on Noise and Vibration Engineering, 2010, pp. 2713–2726.

[33] F.J. Cara, J. Juan, E. Alarcón, E. Reynders, G. De Roeck, Modal contribution and state space order selection in operational modal analysis, Mech. Syst. Signal Process. 38 (2) (2013) 276–298.

[34] E. Orlowitz, A. Brandt, Influence of noise in correlation function estimates for operational modal analysis, in: Topics in Modal Analysis & Testing, Volume 9, Springer, 2019, pp. 55–64.